Optimal X-ray micro-CT image based methods for porosity and permeability quantification in heterogeneous sandstones

by

Ben Callow[1*], Ismael Falcon-Suarez[2], Hector Marin-Moreno[2], Jonathan M. Bull[1] and Sharif Ahmed[3].

May, 2020

(1) University of Southampton, Ocean and Earth Science, Southampton, SO14 3ZH, UK.

(2) National Oceanography Centre, University of Southampton Waterfront Campus, European Way, Southampton, SO14 3ZH, UK.

(3) Diamond Light Source, Oxfordshire, OX11 0DE, UK.

Corresponding author: Ben Callow, University of Southampton, Ocean and Earth Science, Southampton, SO14 3ZH, UK, email: Ben.Callow@noc.soton.ac.uk

Abstract

3D X-ray micro-CT (XCT) is a non-destructive 3D imaging method, increasingly used for a wide range of applications in Earth Science. An optimal XCT image-processing workflow is derived here for accurate quantification of porosity and absolute permeability of heterogeneous sandstone samples using an assessment of key image acquisition and processing parameters: Image resolution, segmentation method, representative elementary volume (REV) size and fluid-simulation method. XCT image-based calculations obtained for heterogeneous sandstones are compared to two homogeneous standards (Berea sandstone and a sphere pack), as well as to the results from physical laboratory measurements. An optimal XCT methodology obtains porosity and permeability results within ± 2% and vary by one order of magnitude around the direct physical measurements, respectively, achieved by incorporating the clay fraction and cement matrix (porous, impermeable components) to the pore-phase for porosity calculations and into the solid-phase for permeability calculations. Two Stokes-flow finite element modelling (FEM) simulation methods, using a voxelised grid (Avizo) and tetrahedral mesh (Comsol) produce comparable results, and similarly show that a lower resolution scan (~5 µm) is unable to resolve the smallest intergranular pores, causing an underestimation of porosity by ~3.5 %. Downsampling the image-resolution post-segmentation (numerical coarsening) and pore network modelling both allow achieving of a representative elementary volume (REV) size, whilst significantly reducing fluid simulation memory requirements. For the heterogeneous sandstones, REV size for permeability (≥ 1 cubic mm) is larger than for porosity (≥ 0.5 cubic mm) due to tortuosity of the fluid paths. This highlights that porosity should not be used as a reference REV for permeability calculations. The findings suggest that distinct image processing workflows for porosity and permeability would significantly enhance the accurate quantification of the two properties from XCT.

Key words: Microstructure, Permeability and porosity, Numerical modelling, Core, Image processing.

1. Introduction

3D X-ray micro-CT imaging (XCT) is a non-destructive, volumetric imaging technique used for understanding the internal structure of materials. XCT has a wide range of applications in Earth Science, including palaeobiology (Tafforeau et al., 2006), volcanology (Zhu et al., 2011), mining (Ghorbani et al., 2011), hydrocarbon recovery and environmental applications such as carbon sequestration (Krevor et al., 2015). XCT for core image analysis has grown in use due to the wider availability of XCT scanners at academic institutions and industrial facilities (Shearing et al., 2018), and the easier access to high memory workstations and supercomputers, capable of performing the calculations required for 3D reconstruction and image processing of large tomographic datasets. Synchrotron-based X-ray sources are becoming more greatly accessible, which produce faster scans at high resolution and phase contrast, generating higher quality images (Fusseis et al., 2014).

A number of standard physical laboratory methods can be used for quantifying the porosity and absolute permeability of rock samples, such us He-pycnometry, Hg-porosimetry and N_2-permeability. Each method introduces uncertainties derived from the testing procedure and the accuracy of the sensors used. For instance, for permeability measurements, rock plugs have to be subjected to a minimum confining stress to ensure advective gas/water flow (e.g., Falcon-Suarez et al., 2018), which may particularly affect measurements for unconsolidated samples. Furthermore, these tests are intrusive and can partially alter the original sample properties, including dissolution/precipitation effects during permeability to water/brine tests (e.g., Canal et al., 2012), incongruencies due to slip-flow effects between gas and water flow-through (Tanikawa and Shimamoto, 2009), or the inability to reuse samples after mercury porosimetry (Falcon-Suarez et al., 2018, Tanikawa and Shimamoto, 2009, Pittman, 1992).

XCT analysis is a non-destructive technique, which allows a greater understanding of why porosity-permeability variations exist in each sample, due to detailed visualisation of the pore- and grain-size distributions and orientations. XCT core image processing and analysis can be performed to calculate the physical properties of rocks and sediment (e.g. Callow et al., 2018). There is a common trade-off between image resolution and sample volume, which can lead to induced error and uncertainties of the calculations. However, robust XCT image processing workflows and pipelines can be used to optimise the accuracy, repeatability and computational efficiency of the calculated physical properties (e.g. Berg et al., 2018).

Porosity and permeability of rock is determined using XCT image processing by classifying the rock into solid- and pore-phases. However, accurately distinguishing between solid and pore (void space) phases in granular materials that contain clays, cements and metastable solids able to precipitate in the pores (e.g., salt or hydrate), becomes more challenging. All natural sediments have some degree of heterogeneity, determined by complex variations in sediment erosion, transport, deposition and diagenetic processes, resulting in grain size and compositional variability (Worden and Burley, 2003). The majority of previous XCT-derived porosity-permeability assessment studies focus on the analysis of homogeneous sandstone samples for determining optimal image processing pipelines (e.g., Mostaghimi et al., 2013; Andra et al., 2013b; Saxena et al., 2017a). The degree of homogeneity is defined by the grain uniformity and pore size distribution, as well as the reduced proportion of clays and cement matrix. However, heterogeneous samples with a wider grain size range, a large proportion of clays and cement matrix, are more susceptible to errors associated with image processing. Heterogeneous samples may also demonstrate a greater spatial variation of measured physical properties. However, it remains unassessed the extent to which the image processing techniques used for porosity and permeability determinations of homogeneous sandstones can be readily applied to more heterogeneous samples.

The main sources of error and uncertainty for XCT image acquisition and processing are derived from the image resolution, image segmentation method, representative elementary volume (REV) size and the fluid flow simulation method. Image spatial resolution dictates the smallest feature that can be visually resolved and identified, which has been previously addressed by a number of authors using compositionally homogeneous sandstone samples (e.g. Saxena et al., 2017; Soulaine et al., 2016; Shah et al., 2016). Ideally, samples would be imaged at the highest image resolution and for the largest possible sample diameter. However, XCT imaging is limited to a length-scale which represents a trade-off between achievable image resolution and imageable sample diameter (Cnudde and Boone, 2013). This trade-off creates errors associated with image resolution, REV size and segmentation. Image resolution and REV can be defined as functions of average pore throat diameter (D_d) and effective grain size (D_{eff}), respectively, for suitable comparisons between samples with varied grain and pore size distributions, as well as comparisons with other digital rock physics (DRP) studies (Eq. 1-2).

$$N_I = \frac{D_d}{\Delta x} \tag{1}$$

$$N_{REV} = \frac{L}{D_{eff}} \tag{2}$$

Where N_I is the ratio of D_d to voxel size (Δx), whilst N_{REV} is the ratio of the cubic length of the sample (L) to D_{eff}. A N_{REV} value of one is equivalent to one grain diameter. For more homogeneous sandstones, a study by Saxena et al. (2018) showed that N_I values above 10 and N_{REV} values above five are required to accurately resolve the smallest pore throat diameters and achieve representative porosity-permeability calculations, respectively.

Image segmentation is the process used to separate and distinguish between the solid and pore (including fluid) phases. A large number of segmentation methods are available (Iassonov et al., 2009, Schlüter et al., 2014), though this study focuses on the use of a 3D weka segmentation method which utilises open-source software, is adaptable and is computationally efficient (Arganda-Carreras et al., 2017). The Trainable Weka segmentation method performed the best in an independent study of seven different segmentation methods, conducted by Berg et al. (2018). When quantifying the porosity and permeability of a rock sample, the REV size is the volume above which the derived porosity-permeability values no longer change significantly (Bear, 2018). Sample REV has also been previously addressed by multiple authors for more compositionally homogeneous sandstone (Ovaysi et al., 2014, Saxena et al., 2018, Mostaghimi et al., 2013).

The lack of a standardized single method for quantifying permeability using XCT image-based technology has triggered the development of a number of flow solvers, which include both commercial and open source softwares. The software may be categorised into Voxel Based Solvers (VBS) and Lattice-Boltzmann Method (LBM) solvers. This study focuses on the former, and compares two Stokes-flow finite element modelling (FEM) methods for calculation of permeability: A voxelised grid (Avizo) and tetrahedral mesh (Comsol). Additionally, this study also calculates permeability quantified and upscaled using pore network modelling (Avizo) and MATLAB Reservoir Simulation toolbox (MRST), respectively.

The ultimate aim of this study is to devise a reliable, repeatable, computationally efficient and robust XCT image processing methodology for the quantification of porosity and permeability of heterogeneous sandstones. To do this, we present an assessment of the main XCT image acquisition and processing parameters using four heterogeneous sandstone samples, which are compared to two homogeneous standards (Berea sandstone and a sphere pack), to understand the sensitivity of the porosity and permeability outputs to each parameter. We then compare four different image-based methods used to quantify permeability, to determine their validity and accuracy. The XCT results are also compared to laboratory physical measurements acquired from the same sample block (twin samples) and compared to the XCT results.

2. Materials and Methods

2.1. Sample description

The samples used in this study consist of two homogeneous sandstones (St1 - Berea sandstone, and St2 - a sphere pack acquired from Andra et al. (2013a)) and four heterogeneous sandstones (A, A2, B and C) collected from a geological field site in Panoche Hills, California, USA (Vigorito and Hurst, 2010). The main component of the samples A-C were quartz mineral grains and a clay mineral fraction. Samples A, A2 and B are uncemented and C is cemented with silica (Opal-CT) (Figure 1). All samples were imaged using a laboratory scanner and subjected to physical laboratory tests (except for St2 and A2).

For the physical laboratory tests, 25 mm length, 50 mm diameter samples were cored from a sample block representative of the samples A, B and C (Figure 1). Each sample was first oven-dried (at 50 °C), before being used to determine porosity by He-pycnometry and permeability to nitrogen (i.e., absolute permeability) under minimal confining pressure conditions (~0.8 MPa). Both determinations were repeated three times per sample. Thereafter, we refer to these tests as physical measurements. For the

XCT study, 25 mm length, 10-12 mm diameter samples were also prepared from the same precursor sample blocks (Figure 1).

2.2. X-Ray Micro-CT analysis

2.2.1. Image acquisition and reconstruction

3D X-ray micro-CT (XCT) scans of samples A-C were conducted using synchrotron X-ray imaging (Figure 2)(Bodey and Rau, 2017). The synchrotron has a parallel beam X-ray source. The specimens were pre-mounted on Scanning Electron Microscopy (SEM) stubs. The SEM stub holder at I13-2 was used to place the specimens in the path of the X-ray beam (Figure 2).

3D reconstruction of the projections was performed using python-based Savu (Atwood et al., 2015). The reconstructed data for samples A-C had an isometric voxel size of 0.81 μm, while for St1 and St2 had a size of 5 μm and 3.5 μm, respectively (Figure 3). The sample volumes A-C are further processed using open-source software Fiji (ImageJ) (Schindelin et al., 2012). Following conversion from 32 bit to 8-bit greyscale data, 1728 voxel (1.4 mm in length) cubic volumes were extracted from each cylindrical sample for further analysis (Figure 2d). The reconstruction method used ensured the minimal presence of noise, blurring and imaging artefacts, which may have effected the accuracy of the subsequent image segmentation process (Figure 2c,d). See Appendix A for further details of the image acquisition and reconstruction process.

2.2.2. Image segmentation

Image segmentation is conducted to isolate and characterise the pore phase. Image segmentation is often challenging due to the partial volume effect, where boundaries between phases in an image are blurred to an amount directly dependent on resolution size (Wildenschild and Sheppard, 2013). Prior to image segmentation, a non-local means filter was applied to the sandstone sub-volumes (Avizo, 2018). The use of a non-local means filter ensures the removal of white noise (scatter), a common noise artefact generated by Compton scattering, while preserving boundary edges (Buades et al., 2005, Ketcham and

Carlson, 2001). The samples A-C are comprised of a solid phase, which includes quartz, feldspar and lithic grains, and a pore phase. Two additional solid components are present and distinguishable, comprising clay minerals and a cement matrix. The clay mineral and cement matrix components are initially assumed to have zero intragranular porosity, so are added to the solid phase.

Image segmentation was conducted using a 3D Weka segmentation (TWS) method (Arganda-Carreras et al., 2017), a machine-learning tool which is built into Fiji. The TWS involved training a classifier using a small number of manual annotations of the two main phases (solid and pore) on a small sub-volume (100 cubic voxels) of sample A. An iterative approach was adopted until an accurate segmentation result was achieved on the sample sub-volume using the Weka training features structure, edges, mean and variance (Rao and Schunck, 1991, Canny, 1986). The structure and edges training features used FeatureJ (Meijering, 2019). The trained classifier was then used to automatically segment samples A-C. A tiling algorithm was adopted to ensure an efficient segmentation on 3D datasets (Arganda-Carreras, 2018), formely a limitation of this segmentation method (Garfi et al., 2019; Berg et al., 2018). The selected tile size dictates the memory requirements of the segmentation. For example, a tile size factor of six divides the volume into 216 (6^3) cubic subvolumes, reducing the memory requirements by a factor of 216. The final segmentation results are qualitatively displayed in Figure 3. Furthermore, a watershed segmentation method (Beucher, 1992) was also used when assessing the effect of changing image resolution.

2.2.3. Pore properties

Voxels assigned to the pore phase define the total porosity and voxels assigned to the pore phase which are connected by a common face define the connected (effective) porosity of the samples. Total porosity can be quantified from the segmented images of the pore space as follows:

$$\emptyset_t = \left(\frac{V_{void}}{V_{ROI}}\right) \times 100 \qquad (3)$$

Where $\emptyset_t$ is total porosity, V_{void} is total void space volume and V_{ROI} is total region of interest (ROI) volume.

A pore network model can be generated using two main methods: A maximal ball method (Dong and Blunt, 2009) and a distance ordered homotopic thinning method (Youssef et al., 2007), this study uses the later to quantify pore throat diameter (D_d). Using a skeletonization algorithm in Avizo, a one voxel thick, centred, homotopic skeleton is created, which is subsequently separated into individual pore segments to produce a pore network model. As D_d was measured using image based methods, whereby D_d is directly dependent on voxel size, the measured D_d of samples A-C (average 25 μm) represents an upper estimate of true pore throat diameter (Saxena et al., 2019a). In addition, effective grain size diameter (D_{eff}) was quantified in 3D using a watershed separation method of the segmented image volumes in Avizo. Accurate quantification of grain size was validated with the Berea sandstone sample (St1), as well as standard (St2) of known grain diameter (100 voxels). A 3D quantification of grain size was preferred to a 2D method, as the later resulted in significant inaccuracies (see Appendix C - Supplementary data; Van Dalen and Koster, 2012).

Table 1 shows the maximum sample dimensions, porosity, effective grain size diameter (D_{eff}) and pore throat sizes (D_d) for the homogeneous sandstone samples (St1-2) and the heterogeneous sandstone samples (A-C). The heterogeneous samples have lower D_{eff} and D_d values relative to the homogeneous sandstones, with a greater percentage of lower grain size fractions (Figure 4). To assess a REV size for quantifying porosity and permeability, sample lengths ranging from 0.04 to 1.4 mm (N_{REV} of >0-10) and 0.04 to 0.5 mm (N_{REV} of >0-3.5) were used repectively (Figure 5). In addition, sample lengths up to 2.5 mm (N_{REV} of $\leq$ 13) were used to assess REV sizes for porosity and permeability for samples St1-2. Two different subsampling strategies are used for the REV analysis: A nested volume sequence (Figure 5a-b) and a cartesian grid of 0.5 mm (N_{REV} = 3.5) subvolumes (Figure 5c-d). Morphology-based methods are not considered in this study due to computational constraints. A sample volume of 600^3 voxels, independent of voxel size, represents the largest volume resolvable using the Stokes-flow simulation methods for all samples within the computer memory limitations of this study (See Appendix B for the computer specifications used for this study).

To understand the effect of varying image resolution on the output values of porosity and permeability, the reconstructed 8-bit grey-scale images for samples A-C were coarsened by a factor of six, creating

XCT images with a 5 μm (4.86 μm) voxel size (Figure 6). Downsampling to a resolution of 5 μm was used for comparison, as this is the resolution achievable using a conventional laboratory X-ray micro-CT scanner with 2000 x 2000 pixel detector elements, for a sample diameter of 10 mm (du Plessis et al., 2017). The 5 μm resolution images are segmented using manual annotations of the new 5 μm image, as well as with the same 3D weka classifier trained using the 1 μm (0.81 μm) voxel size images for direct comparison (Figure 6).

2.2.4. Absolute permeability simulations – Voxelised grid (Avizo)

Absolute permeability, the ability of a porous media to transmit a single-phase fluid, is an intrinsic property of the porous medium that can vary depending on the direction of flow. Herein, absolute permeability will be referred to as permeability. The Avizo 9.3.0 software has been used for quantifying vertical (k_v) and horizontal (k_h) permeability of the connected pore networks of each sample by applying a finite element image-based simulation method (Avizo, 2018). For this method, each voxel corresponds to one mesh element, thus no additional meshing process is required (Zhang et al., 2012). The simulation method has been previously validated using a glass bead pack and theoretical models (Zhang et al., 2011), and successfully applied in previous studies (e.g., Callow et al., 2018, Peng et al., 2014, 2015). Bernard et al. (2005) developed the basis for the permeability simulation algorithm. The velocity of the simulated fluid flow through the sample is calculated by solving the Stokes flow equation:

$$\left.\begin{aligned} \mu\nabla^2\mathbf{u} - \nabla \mathrm{p} = 0 \\ \nabla\cdot\mathbf{u} = 0 \end{aligned}\right\} \quad (4)$$

where $\mathbf{u}$ is the fluid velocity vector, p is the simulated fluid pressure and μ is the dynamic viscosity of the fluid.

Once Eq. (4) is solved through convergence of the simulation and the volumetric flow rate (Q) is calculated, the permeability (k) can be estimated from Darcy's law:

$$\boldsymbol{k} = \frac{\boldsymbol{\mu L Q}}{\boldsymbol{\Delta P A}} \quad \mathbf{(5)}$$

where L is the sample length in the flow direction, Q is the volumetric flow rate, ΔP is the pressure difference across the sample and A is the cross sectional area. For the experimental design, additional volume is added onto the two sample faces that are perpendicular to the main flow direction (Avizo, 2018). This ensures the simulated fluid can spread freely onto the input face of the sample volume, referred to herein as experimental setups (Avizo, 2018). The purpose of the experimental setups are to generate a stabilisation zone where pressure is quasi static. See Appendix B for further details.

2.2.5. Absolute permeability simulation – Tetrahedral mesh (Comsol)

The Comsol permeability simulation uses the creeping flow physics module, which uses a variation of the Stokes flow equation (Eq. 4). The boundary conditions used are the same as for the Avizo simulation. A fully-coupled direct solver was used to quantify fluid flow, and then permeability was calculated using Darcy's law (Eq. 5).

To quantify permeability using the Comsol multiphysics software (Comsol, 2018) a finite element tetrahedral mesh was used. Tetrahedral mesh grids were generated for the segmented pore phase using both Avizo and ScanIP software (Avizo, 2018; Simpleware, 2019). Firstly, a surface of 2D triangular elements is generated on the walls of the voxelised pore volume. Secondly, surface quality tests are performed to check the following properties: 1) Intersection of elements; 2) orientation of elements; 3) closedness of the surface; 4) dihedral angle of elements; and 5) aspect ratio (see Avizo, 2018; Simpleware, 2019 for further details). Finally, a 3D tetrahedral mesh grid is generated from the 2D surface.

In addition, boundary layer elements can be applied to a mesh grid, which are layers of anisotropic hexahedral mesh elements of constant thickness at the walls of the pore-solid interface. Boundary layers are commonly applied in computational fluid dynamic (CFD) simulations to more accurately resolve curved walls with defined boundary conditions.

The number of mesh elements per unit volume (mesh density) can influence the output value of absolute permeability. The number of mesh elements used for a sample volume can be defined as:

$$N_{MESH} = \frac{E_l}{\Delta x} \quad (6)$$

where E_l is the mean edge length of a tetrahedral mesh element and Δx is the image voxel size. Decreasing values of N_{MESH} correspond to an increased mesh element density. A N_{MESH} value of one represents a sample volume with tetrahedral elements equal in length to the image voxel size.

A test varying the N_{MESH} value of a tetrahedral mesh grid of sample St1 was conducted to observe the effect on permeability (Figure 7). The test was performed on a 100^3 voxel subvolume (N_{REV} of 2.6), with and without a boundary layer (Figure 7). Without a boundary layer, a difference of 30 millidarcy (mD), equivalent to a 10 % error, was observed between the highest and lowest N_{MESH} value, equivalent to ~50,000 and ~350,000 mesh elements respectively (Figure 7). A difference of up to 20 mD was observed between the mesh grids generated by Avizo and ScanIP software. A mesh composing of one boundary layer is optimal, as permeability is independent of the number of mesh elements (Figure 7). However, due to the complexity of the pore network geometry, boundary layers using ScanIP and Avizo software are only possible on volumes with less than 150^3 voxels; unless you apply a gaussian filter to the segmented volume, which greatly simplifies the pore network geometry. For this study, mesh grids with a N_{MESH} of 2.6 and no boundary layer were used (Figure 7), due to computer memory limitations and sample volume size constraints.

2.2.6. Absolute permeability simulation – Upscaling (MRST)

Absolute permeability calculations have also been determined in this study using MATLAB Reservoir Simulation Toolbox (MRST)(Lie, 2019). Within this software package, predefined porosity-permeability values can be assigned to cells of a cartesian grid to determine single upscaled calculations. An adapted version of the MRST single-phase upscaling module has been used in this study (Lie, 2019).

2.2.7. Absolute permeability simulation – Pore network model (Avizo)

Further to the pore network model (PNM) generation process described above, PNM's can also be used for calculation of absolute permeability (e.g. Zahasky et al., 2020; Raeini et al., 2019). PNM's for permeability calculation are being used increasingly due to their improved computational efficiency compared to conventional FEM solvers (Raeini et al., 2019).

The number of individual pore segments the connected pore volume are separated into may influence the output value of permeability (known in Avizo as the marker extent). Therefore, it is advisable to calibrate the degree of pore separation until an absolute permeability value is obtained that is comparable to the FEM methods, which can be done on a small sample subvolume (i.e. less than 400^3 voxels). A marker extent of four was used for the samples in this study.

The permeability of the network is calculated using Darcy's law (Eq. 5), whereby total flow rate is deduced from a linear system of equations of flow rate between each pore:

$$Q = \sum(Pi - Pj)g_{ij} \tag{7}$$

where Q is the volumetric flow rate, P is the pressure in each pore pair i,j and g_{ij} is the hydraulic conductance of the throat between each pore pair i,j, given by:

$$g_{ij} = \left(\frac{\pi\, r_{ij}^4}{8\mu l_{ij}}\right) \tag{8}$$

where μ is fluid viscosity, and the throats are represented by cylindrical pipes of radius r and length l between each pore pair i,j.

It is assumed that the PNM is filled with a single-phase, incompressible fluid, with steady state, laminar flow, with mass conservation for each pore body (Avizo, 2018).

3. Results

3.1. X-Ray micro-CT results

3.1.1. Absolute Permeability Simulation Comparison: Avizo vs Comsol

The Avizo and Comsol finite-element fluid simulation methods, using a voxelised grid and tetrahedral mesh respectively, are directly compared (Figure 8). Figure 9 shows good correlations for both the Avizo and Comsol simulations with slight deviations in the latter case. Slight permeability underestimations for the Comsol simulation relative to Avizo within the 1-1000 mD range can be explained by the selected mesh used for the simulations (N_{MESH} of 2.6 with no mesh boundary layer) (Figure 7).

Apparent overestimations of permeability by the Comsol simulations are observed within the 1000-10000 mD range for sample A2. The apparent discrepancy between the two simulation methods observed within the 1000-10000 mD range cannot be explained by the selected mesh grid properties, which lie within an uncertainty range of 10-20 % (0.1-0.2). For the three subvolumes that display the anomalous permeability values, where permeability (k) has been simulated in three planes of direction (subscripts x,y and z), k_y has an error below 50 % (0.5), whereas errors above 200% are observed for k_x and k_z (2). The sample faces perpendicular to the main flow direction for the k_x and k_z simulation have pore volume across the entire input and output faces. The Comsol simulation does not have experimental setups added onto the faces perpendicular to the main inflow and outflow direction, to ensure that the simulation achieves a quasi-static pressure state. Therefore, the lack of experimental setups is likely the cause of the error.

3.1.2. Representative Elementary Volume REV and Image Resolution

3.1.2.1. Porosity and Permeability REV

Using a nested volume sequence (Figure 5a-b), porosity calculations appear to be resolved at N_{REV} values ≥ 5 for all samples (equivalent to sample lengths ≥ 0.5 mm for A-C) (Figure 10). Permeability measurements appear to be resolved at $N_{REV} \geq 3.5$ for samples A-C and $N_{REV} \geq 5$ for samples St1-2 (equivalent to sample lengths ≥ 0.4 mm and ≥ 1 mm, respectively). Therefore, sample lengths of N_{REV} ≥ 5 can be considered a REV size for permeability for homogeneous sandstone. To observe a lower permeability REV size for heterogeneous sandstone samples compared to more homogeneous sandstones would be highly unexpected. Therefore, the REV size for permeability calculations may not be accurately determined from one sub-volume for samples A-C, so a larger number of subvolumes will be further analysed.

Using a cartesian grid of subvolumes (Figure 5c-d), sample St1 subvolumes lie within a narrow permeability range of 421- 467 mD and porosity variations of ± 1.1 % when using sample lengths of $N_{REV} \geq 10$ (2.5 mm length) (omitting one outlier; Figure 11). Conversely, sample lengths equivalent to $N_{REV} \geq 3.5$ (>0.5 mm length) for samples A-C display variations of permeability over two orders of magnitude and porosity up to ± 16.8 % (Figure 11). The large scattering shown by samples A-C suggest that using only one sub-volume of sample length equivalent to $N_{REV} \geq 3.5$ is an inadequate permeability REV size for the heterogeneous sandstone cases.

For samples A-C, linear best fits are plotted for permeability in the vertical (k_v) and horizontal (k_h) directions, to obtain estimates for each sample using the known connected porosity (Øc) calculated from the maximum sample volume size ($N_{REV} \geq 10$; Figure 11). The interpolated permeability values from the porosity-permeability curves are shown in Table 2.

The cartesian grid of subvolumes have also been put in MRST. Upscaled permeability calculations are obtained for the volume averaged arithmetic, arithmetic-harmonic and harmonic means, respectively (Table 3; Appendix C - supplementary figure; Lie, 2019). In fluid mechanics, harmonic and arithmetic averaging are considered the correct method of upscaling in a stratified isotropic medium with layers perpendicular and parallel to the direction of pressure drop, respectively. The calculated arithmetic mean closely matches the interpolated permeability values (within 3-23 mD)(Table 3).

The effect of downsampling image resolution for samples A-C is also assessed (Figure 12). The TWS method has been used to segment the downsampled 5 µm images and classify the solid and pore phases using manual annotations of the 5 µm images. Compared to calculations at the original resolution (0.81 µm), porosity is underestimated by ≤ 3.5 % (Figure 12). Permeability values are also slightly underestimated by ≤ 16 mD, with the exception of sample C which overestimates permeability by 83 mD. These slight underestimations may be due to incorrect classification of the pore phase at 5 µm voxel resolution, highlighting the importance of having sufficient image resolution to accurately segment and classify the smallest pores. The higher permeability calculated for sample C may also be explained by the omission of the smallest pore throats.

Furthermore, when applying the TWS method, a new trained classifier is required for sample images scanned at two different image resolutions. Where the classifier trained for the 1 µm images is applied to the 5 µm images, significant inaccuracies are observed, with porosity and permeability variations of up to 10 % and two orders of magnitude, respectively (Figure 12).

3.2. Laboratory physical measurements vs X-ray micro-CT

The interpolated XCT permeability values (Table 2) vary by one order of magnitude around the physical measurements (Table 4). However, the physical porosity measurements are up to 18.3 % higher than the total porosity obtained using XCT (Table 4). This large discrepancy is likely related to the intragranular porosity fraction of the clays and cement matrix in the samples. The presence of intragranular porosity for the clays and cement matrix, which lays below the resolution of the XCT image, was assigned to the solid phase for the original XCT image analysis. Reassigning part of the mineral clay fraction and cement matrix to the pore phase produce XCT total porosity values which closely match the physical measurements (Appendix C - supplementary figure). For this calculation, it is assumed that clay and silica (Opal-CT) cement contain up to 60 % and 70% intragranular porosity, respectively, which aligns with upper estimates derived from previous studies (Hurst and Nadeau, 1995, Alansari et al., 2019), as well as mass balance considerations used in this study (Appendix C - supplementary data).

4. Discussion

4.1. Absolute Permeability Simulation Comparison: Avizo vs Comsol softwares

The two simulations are comparable for the 1-1000 mD range. The overestimation of permeability using the Comsol Stokes-flow simulation within the 1000-10000 mD range evidences the importance of the experimental setup added to the inflow and outflow direction for the Avizo simulation, which is used to achieve a quasi-static pressure state at the input and output faces of the sample volume.

The error of 20% induced by the chosen N_{MESH} (mesh density) value could be mitigated by reducing the N_{MESH} value, but this significantly increases the computational requirements of the simulation. The error could also be mitigated by introducing a boundary layer to the mesh (Figure 7). However, a boundary layer for complex pore geometries and for volume sizes >150^3 voxels cannot be generated without simplifying the pore geometry using a gaussian filter (Bird et al., 2014). This study suggests a finite element solver not requiring an additional meshing process would be a preferred simulation method due to the increased time efficiency and the omittance of a mesh density (N_{MESH}) induced error. The ability to introduce experimental setups for the creeping flow module in Comsol may also greatly improve the accuracy of the permeability calculations using this method.

4.2. Representative Elementary Volume versus Image Resolution

Saxena et al. (2018) show that for homogeneous sandstones a N_I value > 10 is required to accurately resolve the smallest pores. For a N_I value of 10, the upper limit of voxel size required to resolve the dominant pore throats is 2.5 µm for heterogenous samples A-C (Eq.2), which is achieved in this study (0.81 µm). At a resolution of 0.81 µm, the maximum N_{REV} achievable is 3.5. However for the downsampled image at 5 µm, the maximum N_I value is 5. This study has shown that acquiring XCT image scans at a lower resolution (i.e. N_I < 10) will lead to an underestimation of porosity (Figure 12). An important aspect to consider is microporosity, defined here as intergranular porosity lying below sub-voxel resolution. The quantification of microporosity for samples A-C at 5 µm resolution is ≤ 3.5 %, but is unclear for 1 µm resolution. Shah et al. (2016) and Saxena et al. (2017b) show up to ± 4 % of the total porosity attributed to the microporosity fraction is commonly omitted when compared to the true porosity of the samples if image acquisition is conducted at a lower resolution, in agreement with our study. This error range is also within the limits observed in this study when using a watershed segmentation technique (Appendix C – supplementary data).

This study shows that using a 3D weka segmentation technique produces accurate segmentation results, in agreement with Berg et al. (2018), but shows the image classifiers are highly sensitive to changes in greyscale image resolution (Figure 12). The same trained classifier can be applied to sample images that have comparable petrophysical properties, and are obtained using the same image acquisition parameters, spatial resolution and reconstruction process. At a single image resolution, samples A, A2 and B used the same trained classifier. These are important considerations for future machine-learning based image segmentation studies.

This study has also shown that acquiring XCT image scans at a lower resolution may lead to slight underestimations of permeability. This directly contrasts studies conducted on homogeneous sandstones such as Saxena et al. (2018), which commonly show that lower resolution leads to overestimations of permeability, in agreement with calculations of sample B. Overestimations occur as the smallest pores are uresolved, leading to an increased flow velocity through the porous media. Overall, permeability values at 1 µm and 5 µm are in close agreement (Figure 12).

This study shows a lower REV for porosity than for permeability, which is in agreement with Mostaghimi et al. (2013) and Saxena et al. (2018). A larger REV may be required for permeability, in order to incorporate a suitable amount of tortuosity into the simulation. From Figure 10, it appeared that for samples A-C, a REV size may be achieved due to the apparent lowered change in permeability with increased sample length up to a N_{REV} of 3.5. Coefficient of variation (COV) is used as a statistical measure of determining whether a REV size is achieved for permeability calculations. A COV (100 x standard deviation/mean) percentage value of less than 15 % is determined to be representative (Saxena et al., 2018). Shown in this study and Saxena et al. (2018), for homogeneous samples a N_{REV} of > 5 achieves a COV % of < 15 %, showing that a REV is achieved (Figure 11). However, for the heterogeneous samples (A-C) at a N_{REV} of 3.5, the COV values are 98 %, 89 % and 177 %, respectively (Figure 11). These values far exceed the COV % values required to achieve a REV size. Therefore, to overcome the trade off between N_I and N_{REV}, further image processing is conducted.

Quantifying permeability is much more computationally intensive than porosity using XCT images, as the fluid flow simulations require high computer memory. The best solution for obtaining REV permeability measurements whilst preserving image resolution is to downsample the XCT image volume post-segmentation, referred to herein as numerical coarsening (NC) (Figure 13). Shah et al. (2016) showed that numerical coarsening may be an effective solution. NC by a factor of three allows the full 1.4 mm length sample volume to be simulated (N_{REV} of 10) without inducing significant changes to the pore network geometry (Figure 13). The results of NC are summarised in Table 5. Quantitatively, minor permeability changes are observed for a NC factor of 3-8 (≤ ±50 mD), while porosity reduces linearly below 2 %. The interpolated values of porosity-permeability, acquired from the plots of 27 subvolumes (Table 2) closely match the permeability values obtained from numerical coarsening (NC). For samples A, A2, B and C a revised N_{REV} of ≥ 7 is determined (Figure 13). The simple process of NC allows permeability to be quantified on a more representative elementary volume (REV) size without compromising the accuracy of the result, whilst reducing processing time by a factor of ~ 500 (20 times faster simulation and 26 times less voxel volumes required).

Another solution for obtaining REV permeability calculations whilst preserving image resolution is to simplify the pore geometry using pore network modelling (PNM). Permeability calculations using a PNM of the full 1.4 mm length sample volumes (N_{REV} of 10) correlate well with the calculations determined using numerical coarsening (NC), and also determine a N_{REV} of ≥ 7 for samples A, A2, B and C (Figure 13).

4.3. Comparison of physical measurement and X-ray micro-CT image-based methods

The major discrepancy between the XCT analysis and physical measurements was the original difference in total porosity (up to ± 18.3 %). Pore space within the clay mineral fraction and cement matrix is highly dominated by non-connected/disconnected intragranular pores (Hay et al., 2011, Milliken and Curtis, 2016). Therefore, when computing porosity from XCT, the clay mineral fraction and cement matrix should be assigned to the pore phase. Table 6 shows porosity and permeability output for re-segmented XCT images, whereby clay minerals and cement matrix are assigned to the pore phase (Appendix C – supplementary figure). By doing this, the computed porosity is closer to the physical measurement of porosity (within ± 2 %). For the revised total porosity calculations, the clay minerals and cement matrix are estimated to contain 60 % and 70 % intragranular porosity respectively, based on literature estimates (Hurst and Nadeau, 1995, Alansari et al., 2019) and mass balance considerations (Appendix C – supplementary data). Menke et al. (2019) and Lin et al. (2016) demonstrated that conducting two scans, differential imaging of a dry scan and brine saturated scan, can be used to determine sub-resolution microporosity. Future studies to quantify the precise intragranular microporosity of different clay minerals and cement types will be required, if XCT is to be used as the primary method for total porosity calculations of heterogeneous sandstone samples.

The intermediate phase of rock and sediment sample scans is commonly assumed to be comprised of sub-resolution intergranular pores, connected to the connected macro-pore volume (e.g. Soulaine et al. 2016; Lin et al. 2016; Bultreys et al., 2015). However, for heterogeneous sandstones the large proportion of disconnected intragranular clay and cement matrix generates an additional peak within the intermediate phase range. (Appendix C – supplementary figure), therefore it is not reasonable to assume that the grey values between the solid grains and macro pores only consist of sub-resolution connected microporosity. This is demonstrated by using a simple thresholding segmentation. By applying a simple interactive thresholding (or watershed) segmentation technique and assigning the physical measurement of porosity to match the threshold, a segmented image can be created with an identical calculated porosity to the physical measurement, a technique adopted in previous studies (Vogel et al., 2005, Iassonov et al., 2009, Wu et al., 2017). However, when using the same re-segmented volume for permeability, the obtained values are significantly overestimated (by up to two orders of magnitude; Table 6), in agreement with Leu et al. (2014). Therefore, for the calculation of permeability from XCT images of heterogeneous sandstones, the clay minerals and cement matrix should be assigned to the solid phase, as their intragranular pores are non-connected.

For the purposes of this study, the distinction has been made between more homogeneous and heterogeneous sandstones based on the textural and pore properties of the samples. Though, in reality this distinction is not well defined due to the wide spectrum of their petrophysical properties. A porosity of 11.7 % was originally assigned to the Berea sandstone (St1), following an optimal image processing workflow that considered the intermediate clay and cement fractions as part of the solid phase. After reassigning the clay and cement fractions to the pore phase, the porosity increases to 15.82 %, but is still ~4% below the experimental porosity (19.8 %). The ~ 4% underestimation of the total porosity is explained by the spatial resolution of 5 μm used for this sample (Section 4.2; Figure 13b). This observation suggests that for all sandstone sample types, the clay fraction and cement matrix should be assigned to the solid phase for permeability calculations, and to the pore phase for total porosity calculations.

Applying this particular assignment, porosity and permeability can be obtained using XCT with an associated error of ± 2 % and one order of magnitude, respectively, when compared to the physical measurements using standard laboratory testing methods. Therefore, despite an optimal XCT workflow using high resolution and high-phase contrast scans, samples A-C and St1 still show a slight underestimation of total porosity relative to standard laboratory measurements (Figure 14a; Table 7). The porosity underestimation can be explained by a portion of the intergranular microporosity remaining below the maximum voxel resolution (Saxena et al. 2019b). An associated error may also be explained by conservative estimates of the clay and cement intragranular microporosity fractions, and associated mass balance considerations. To further address this uncertainty, previous works have undertaken Hg-injection porosimetry analysis to obtain the pore size distribution and porosity fraction below the maximum image resolution (e.g. Swanson, 2013, Saxena et al., 2019b). Falcon-Suarez et al 2019 report Hg-injection porosimetry analysis for heterogeneous sandstones, which show that up to 25 % of the total porosity is attributed to the combined intergranular and intragranular microporosity fraction (i.e. throat diameter < 1.6 μm). These values further explain the original discrepancy observed between XCT and the physical laboratory measurements, and support the calculation enhancement derived from the proposed (clay fraction and cement matrix) phases reassignment during image segmentation.

The three XCT voxelised grid image-based methods used for permeability calculation (i.e. numerical coarsening, pore network modelling and upscaling using interpolation of multiple subvolumes) show a good agreement (Figure 14b; Table 7). However, an overestimation of permeability for the XCT images relative to the physical measurements is common, despite the implementation of accurate XCT image processing techniques (Saxena et al., 2017a; Figure 14b). One reason for permeability overestimation is the sample volume size. The maximum volume size for the XCT image was 1.4 cubic mm, whereas the volume size of the sample used in the experiment was ~200,000 mm^3. Furthermore, the sample used for the laboratory experiment is ~20 times larger in vertical length (25 mm) than the maximum vertical dimension of the XCT image. The greater length may result in greater tortuosity, which may cause a reduced permeability for the physical measurements, relative to the XCT image-based calculations. From the MRST upscaled calculations, the harmonic mean most closely matches the laboratory measurements. Therefore, over a larger sample volume, the less permeable mm-scale sub-regions may have a greater effect on the output permeability at core scale. Furthermore, this study uses separate samples for the laboratory measurements and XCT calculations, despite being from the same sample block. Therefore, it is likely that heterogeneities (observed even at $N_{REV} > 10$) are contributing to the discrepancies between the XCT calculations and physical measurements. This source of error is less evident where the physical porosity has been measured on identical sub-volumes, demonstrated in a few well controlled studies such as Pini and Madonna (2016) and Jackson et al. (2020).

The small confining pressure of 0.8 Mpa used to conduct the physical measurement is a further reason for the discrepancy between the XCT and physical measurements of permeability. Despite being relatively small, the applied stress may cause closure of microcracks. This alteration of the pore geometry and grain configuration, may be enough to reduce the permeability (e.g., Falcon-Suarez et al., 2017). For our relatively high permeability rocks, this minor low stress-induced microcrack closure is commonly neglected. But here, the results from the physical lab tests are being compared to the high precision XCT method, and therefore any source of permeability fluctuation has to be considered. In this regard, Farrell et al (2014) report data of measurable stress-induced permeability changes in high permeability (cracked) sandstones even for minimal changes in the state of stress. In addition, simple single-phase Stokes-flow simulations omit rock-fluid interactions, such as the effect of clay swelling, further highlighted in previous studies directly comparing XCT and physical laboratory measurement results (Callow et al., 2018). Transform functions could be performed to attempt to fit the XCT image calculations to the laboratory measurements (e.g. Saxena et al., 2019a), though this approach is beyond the scope of this study.

5. Conclusions

This study has addressed the uncertainties associated with 3D X-ray micro-CT (XCT) image processing of heterogeneous sandstones to define an optimal XCT methodology for the quantification of porosity and absolute permeability at the pore scale (Figure 15). Overall, the XCT image-based calculations show good agreement with the physical measurements following careful consideration of the uncertainties associated with the parameters of the XCT image-processing methodology. The main findings of this study are:

- A 3D weka segmentation can accurately distinguish between the solid- and pore- phases. 3D weka classifiers are highly sensitive to changes in image spatial resolution, therefore should only be used on samples acquired using the same scanning acquisition and reconstruction parameters.
- Clay minerals and cement matrix must be assigned to the pore-phase for porosity calculation, and to the solid-phase for permeability calculation, due to the presence of poorly-connected intragranular porosity. Incorrect assignment of the clay minerals and cement matrix can cause porosity underestimations up to 18.3 % and permeability overestimations up to two orders of magnitude. Future work to constrain precise values of clay and cement matrix intragranular microporosity are required to more accurately quantify total porosity using XCT.
- For heterogeneous sandstone rocks considered in this study, representative elementary volume (REV) size for permeability ($N_{REV} > 7$) is larger than for porosity ($N_{REV} > 5$), showing that porosity should not be used as a reference REV for permeability calculations.
- Scannning at a lower image resolution (5 µm compared to 1 µm), can result in underestimation of porosity by up to 3.5 %, due to the inability to resolve and classify pores that are sub-voxel size resolution.
- The use of Stokes-flow simulation results derived from voxelised grids (Avizo) and tetrahedral meshes (Comsol) are in reasonably agreement, though use of meshes that are not fine enough to accurately resolve the flow paths may induce permeability errors of up to 20%. Careful

experimental design is required for the flow simulations, to ensure a quasi-static pressure state at the input and output faces of the sample volumes.

- Results derived from optimal XCT calculations and standard physical laboratory measurements show good agreement, producing porosity and permeability values within ± 2% and one order of magnitude, respectively. Differences in porosity-permeability results between the two methods are predominantly attributed to scaling effects, use of twin samples, as well as the omission of rock-fluid interactions and stress effects in the numerical fluid simulations.

Acknowledgements

We acknowledge funding from the European Union's Horizon 2020 research and innovation programme under grant agreement No. 654462 – STEMM-CCS. We acknowledge Diamond Light Source for time on Beamline I13-2 under Proposal MT18758. We give our thanks to Hans Deyhle, Christina Reinhard, Shashi Marathe, Andrew Bodey and the Diamond Support Scientists at I13-2 for their support during the experiment. We are also very grateful for the advice and guidance with image reconstruction provided by Kaz Wanelik. We acknowledge the use of the IRIDIS High Performance Computing Facility, and associated support services at the University of Southampton, in the completion of this work. We would like to thank our colleagues at the μ-VIS X-Ray Imaging Centre, University of Southampton for their helpful advice and support. We would also like to thank Andrew Hurst and Antonio Grippa (University of Aberdeen, Sand Injection Research Group) for their assistance and advice with fieldwork and rock sampling in California. We would like to thank the FEI Visualization Sciences Group for providing the use of the Avizo 9.3.0 software for X-Ray micro-CT (XCT) image processing, Simpleware for the use of their ScanIP meshing software and Comsol for use of their Multiphysics software. Finally, we would like to sincerely thank Samuel Jackson and two anonymous reviewers for their constructive comments, which greatly improved the manuscript. Author contribution statement: B.C., I.F.S.: Conceptualization, Formal Analysis, Validation. B.C.: Data curation, Methodology, Software, Visualization. B.C., J.M.B., S.A.: Funding acquisition. B.C., I.F.S., H.M.M., S.A.: Investigation. B.C., I.F.S., H.M.M., J.M.B., S.A: Writing. The dataset associated with this work is

available online at https://doi.org/10.5258/SOTON/D1441. Here we provide the raw and segmented X-ray micro-CT tomographic image data, and the associated image processing files.

References

Alansari, A., Salim, A.M.A., Janjuhah, H.T., Bin Abd Rahman, A.H. & Fello, N.M., 2019. Quantification of clay mineral microporosity and its application to water saturation and effective porosity estimation: A case study from Upper Ordovician reservoir, Libya, Journal of Natural Gas Geoscience, 4, 139-150, doi: 10.1016/j.jnggs.2019.04.005.

Andra, H., Combaret, N., Dvorkin, J., Glatt, E., Han, J., Kabel, M., Keehm, Y., Krzikalla, F., Lee, M., Madonna, C., Marsh, M., Mukerji, T., Saenger, E.H., Sain, R., Saxena, N., Ricker, S., Wiegmann, A. & Zhan, X., 2013a. Digital rock physics benchmarks-Part I: Imaging and segmentation, Computers & Geosciences, 50, 25-32, doi: 10.1016/j.cageo.2012.09.005.

Andra, H., Combaret, N., Dvorkin, J., Glatt, E., Han, J., Kabel, M., Keehm, Y., Krzikalla, F., Lee, M., Madonna, C., Marsh, M., Mukerji, T., Saenger, E.H., Sain, R., Saxena, N., Ricker, S., Wiegmann, A. & Zhan, X., 2013b. Digital rock physics benchmarks-part II: Computing effective properties, Computers & Geosciences, 50, 33-43, doi: 10.1016/j.cageo.2012.09.008.

Arganda-Carreras, I., 2018. Weka Segmentation tiling script. https://forum.image.sc/t/trainable-weka-error-large-images/10929 (last accessed 02.10.2019 and script uploaded on 25.05.2018).

Arganda-Carreras, I., Kaynig, V., Rueden, C., Eliceiri, K.W., Schindelin, J., Cardona, A. & Seung, H.S., 2017. Trainable Weka Segmentation: a machine learning tool for microscopy pixel classification, Bioinformatics, 33, 2424-2426, doi: 10.1093/bioinformatics/btx180.

Atwood, R.C., Bodey, A.J., Price, S.W.T., Basham, M. & Drakopoulos, M., 2015. A high-throughput system for high-quality tomographic reconstruction of large datasets at Diamond Light Source, Philosophical Transactions of the Royal Society A: Mathematical, Physical and Engineering Sciences, 373, doi: 10.1098/rsta.2014.0398.

Avizo, 2018. Avizo 3D Software User's Guide. FEI.

https://www.fei.com/software/avizo-user-guide/ (accessed 02.10.2019). in Version 9. 1-967.

Bear, J., 2018a. Modeling Phenomena of Flow and Transport in Porous Media, 31, 1-98, Springer International Publishing, doi: 10.1007/978-3-319-72826-1_1.

Berg, S., Saxena, N., Shaik, M. & Pradhan, C., 2018. Generation of ground truth images to validate micro-CT image-processing pipelines, The Leading Edge, 37, 412-420, doi: 10.1190/tle37060412.1.

Bernard, D., Nielsen, Ø., Salvo, L. & Cloetens, P., 2005. Permeability assessment by 3D interdendritic flow simulations on microtomography mappings of Al–Cu alloys, Materials Science and Engineering: A, 392, 112-120, doi: 10.1016/j.msea.2004.09.004.

Beucher, S., 1992. The watershed transformation applied to image segmentation, Scanning Microscopy-Supplement, 299-299, ISSN: 0892-953X.

Bird, M.B., Butler, S.L., Hawkes, C.D. & Kotzer, T., 2014. Numerical modeling of fluid and electrical currents through geometries based on synchrotron X-ray tomographic images of reservoir rocks using Avizo and COMSOL, Computers & Geosciences, 73, 6-16, doi: 10.1016/j.cageo.2014.08.009.

Bodey, A.J. & Rau, C., 2017. Launch of the I13-2 data beamline at the Diamond Light Source synchrotron, Journal of Physics: Conference Series, 849, 012038, doi: 10.1088/1742-6596/849/1/012038.

Buades, A., Coll, B. & Morel, J.M., 2005. A Non-Local Algorithm for Image Denoising, Proceedings of the 2005 IEEE Computer Society Conference on Computer Vision and Pattern Recognition, 2, 60-65, doi: 10.1109/cvpr.2005.38.

Bultreys, T., Van Hoorebeke, L. & Cnudde, V., 2015. Multi-scale, micro-computed tomography-based pore network models to simulate drainage in heterogeneous rocks, Advances in Water Resources, 78, 36-49, doi: 10.1016/j.advwatres.2015.02.003.

Callow, B., Falcon-Suarez, I., Ahmed, S. & Matter, J., 2018. Assessing the carbon sequestration potential of basalt using X-ray micro-CT and rock mechanics, International Journal of Greenhouse Gas Control, 70, 146-156, doi: 10.1016/j.ijggc.2017.12.008.

Canal, J., Delgado, J., Falcón, I., Yang, Q., Juncosa, R. & Barrientos, V., 2012. Injection of CO2-Saturated Water through a Siliceous Sandstone Plug from the Hontomin Test Site (Spain):

Experiment and Modeling, Environmental Science & Technology, 47, 159-167, doi: 10.1021/es3012222.

Canny, J., 1986. A Computational Approach to Edge Detection, IEEE Transactions on Pattern Analysis and Machine Intelligence, PAMI-8, 679-698, doi: 10.1109/TPAMI.1986.4767851.

Cnudde, V. & Boone, M.N., 2013. High-resolution X-ray computed tomography in geosciences: A review of the current technology and applications, Earth-Science Reviews, 123, 1-17, doi: 10.1016/j.earscirev.2013.04.003.

Comsol, 2018. COMSOL Multiphysics Reference Manual. COMSOL AB. https://doc.comsol.com/5.4/doc/com.comsol.help.comsol/COMSOL_ReferenceManual.pdf (accessed 02.10.2019). in Version 5.4, Stockholm, Sweden.

Dong, H. & Blunt, M.J., 2009. Pore-network extraction from micro-computerized-tomography images, Physical Review E, 80, doi: 10.1103/PhysRevE.80.036307.

du Plessis, A., Broeckhoven, C., Guelpa, A. & le Roux, S.G., 2017. Laboratory x-ray micro-computed tomography: a user guideline for biological samples, GigaScience, 6, doi: 10.1093/gigascience/gix027.

Falcon-Suarez, I., Canal-Vila, J., Delgado-Martin, J., North, L. & Best, A., 2017. Characterisation and multifaceted anisotropy assessment of Corvio sandstone for geological CO2 storage studies, Geophysical Prospecting, 65, 1293-1311, doi: 10.1111/1365-2478.12469.

Falcon-Suarez, I., Papageorgiou, G., Chadwick, A., North, L., Best, A.I. & Chapman, M., 2018. CO2-brine flow-through on an Utsira Sand core sample: Experimental and modelling. Implications for the Sleipner storage field, International Journal of Greenhouse Gas Control, 68, 236-246, doi: 10.1016/j.ijggc.2017.11.019.

Falcon-Suarez, I.H., Amalokwu, K., Delgado-Martin, J., Callow, B., Robert, K., North, L., Sahoo, S.K. & Best, A.I., 2018. Comparison of stress-dependent geophysical, hydraulic and mechanical properties of synthetic and natural sandstones for reservoir characterization and monitoring studies, Geophysical Prospecting, 67, 784-803, doi: 10.1111/1365-2478.12699.

Farrell, N. J. C., Healy, D., & Taylor, C. W. (2014), Anisotropy of permeability in faulted porous sandstones, Journal of Structural Geology, 63, 50-67, doi: 10.1016/j.jsg.2014.02.008.

Fusseis, F., Xiao, X., Schrank, C. & De Carlo, F., 2014. A brief guide to synchrotron radiation-based microtomography in (structural) geology and rock mechanics, Journal of Structural Geology, 65, 1-16, doi: 10.1016/j.jsg.2014.02.005.

Garfi, G., John, C.M., Berg, S. & Krevor, S., 2019. The Sensitivity of Estimates of Multiphase Fluid and Solid Properties of Porous Rocks to Image Processing, Transport in Porous Media, 131, 985-1005, doi: 10.1007/s11242-019-01374-z.

Ghorbani, Y., Becker, M., Petersen, J., Morar, S.H., Mainza, A. & Franzidis, J.P., 2011. Use of X-ray computed tomography to investigate crack distribution and mineral dissemination in sphalerite ore particles, Minerals Engineering, 24, 1249-1257, doi: 10.1016/j.mineng.2011.04.008.

Hay, M.B., Stoliker, D.L., Davis, J.A. & Zachara, J.M., 2011. Characterization of the intragranular water regime within subsurface sediments: Pore volume, surface area, and mass transfer limitations, Water Resources Research, 47, doi: 10.1029/2010WR010303.

Hurst, A. & Nadeau, P.H., 1995. Clay Microporosity in Reservoir Sandstones - an Application of Quantitative Electron-Microscopy in Petrophysical Evaluation, Aapg Bulletin-American Association of Petroleum Geologists, 79, 563-573, doi: 10.1306/8D2B1598-171E-11D7-8645000102C1865D.

Iassonov, P., Gebrenegus, T. & Tuller, M., 2009. Segmentation of X-ray computed tomography images of porous materials: A crucial step for characterization and quantitative analysis of pore structures, Water Resources Research, 45, doi: 10.1029/2009WR008087.

Jackson, S.J., Lin, Q. & Krevor, S., 2020. Representative elementary volumes, hysteresis and heterogeneity in multiphase flow from the pore to continuum scale, Water Resources Research, doi: 10.1029/2019WR026396.

Ketcham, R.A. & Carlson, W.D., 2001. Acquisition, optimization and interpretation of X-ray computed tomographic imagery: applications to the geosciences, Computers & Geosciences, 27, 381-400, doi: 10.1016/S0098-3004(00)00116-3.

Krevor, S., Blunt, M.J., Benson, S.M., Pentland, C.H., Reynolds, C., Al-Menhali, A. & Niu, B., 2015. Capillary trapping for geologic carbon dioxide storage – From pore scale physics to field scale implications, International Journal of Greenhouse Gas Control, 40, 221-237, doi: 10.1016/j.ijggc.2015.04.006.

Leu, L., Berg, S., Enzmann, F., Armstrong, R.T. & Kersten, M., 2014. Fast X-ray Micro-Tomography of Multiphase Flow in Berea Sandstone: A Sensitivity Study on Image Processing, Transport in Porous Media, 105, 451-469, doi: 10.1007/s11242-014-0378-4.

Lie, K.-A, 2019. An Introduction to Reservoir Simulation Using MATLAB/GNU Octave: User Guide for the MATLAB Reservoir Simulation Toolbox (MRST). Cambridge University Press, 2019. www.cambridge.org/9781108492430 (accessed 15.03.2020).

Lin, Q., Al-Khulaifi, Y., Blunt, M.J. & Bijeljic, B., 2016. Quantification of sub-resolution porosity in carbonate rocks by applying high-salinity contrast brine using X-ray microtomography differential imaging, Advances in Water Resources, 96, 306-322, doi: 10.1016/j.advwatres.2016.08.002.

Meijering, E., 2019. FeatureJ: An ImageJ Plugin Suite for Image Feature Extraction. https://imagescience.org/meijering/software/featurej/ (accessed 02.10.2019).

Menke, H., Gao, Y., Linden, S., & Andrew, M., 2019. Using nano-XRM and high-contrast imaging to inform micro-porosity permeability during Stokes-Brinkman single and two-phase flow simulations on micro-CT images. EarthArXiv. IN REVIEW (2019). https://doi.org/10.31223/osf.io/ubg6p.

Milliken, K.L. & Curtis, M.E., 2016. Imaging pores in sedimentary rocks: Foundation of porosity prediction, Marine and Petroleum Geology, 73, 590-608, doi: 10.1016/j.marpetgeo.2016.03.020.

Mostaghimi, P., Blunt, M.J. & Bijeljic, B., 2013. Computations of Absolute Permeability on Micro-CT Images, Mathematical Geosciences, 45, 103-125, doi: 10.1007/s11004-012-9431-4.

Ovaysi, S., Wheeler, M.F. & Balhoff, M., 2014. Quantifying the Representative Size in Porous Media, Transport in Porous Media, 104, 349-362, doi: 10.1007/s11242-014-0338-z.

Peng, S., Marone, F. & Dultz, S., 2014. Resolution effect in X-ray microcomputed tomography imaging and small pore's contribution to permeability for a Berea sandstone, Journal of Hydrology, 510, 403-411, doi: 10.1016/j.jhydrol.2013.12.028.

Peng, S., Yang, J.J., Xiao, X.H., Loucks, B., Ruppel, S.C. & Zhang, T.W., 2015. An Integrated Method for Upscaling Pore-Network Characterization and Permeability Estimation: Example from the Mississippian Barnett Shale, Transport in Porous Media, 109, 359-376, doi: 10.1007/s11242-015-0523-8.

Pini, R. & Madonna, C., 2016. Moving across scales: a quantitative assessment of X-ray CT to measure the porosity of rocks, Journal of Porous Materials, 23, 325-338, doi: 10.1007/s10934-015-0085-8.

Pittman, E.D., 1992. Relationship of porosity and permeability to various parameters derived from mercury injection-capillary pressure curves for sandstone, AAPG bulletin, 76, 191-198, ISSN: 0149-1423

Raeini, A.Q., Yang, J., Bondino, I., Bultreys, T., Blunt, M.J. & Bijeljic, B., 2019. Validating the Generalized Pore Network Model Using Micro-CT Images of Two-Phase Flow, Transport in Porous Media, 130, 405-424, doi: 10.1007/s11242-019-01317-8.

Rao, A.R. & Schunck, B.G., 1991. Computing oriented texture fields, CVGIP: Graphical Models and Image Processing, 53, 157-185, doi: 10.1016/1049-9652(91)90059-S.

Saxena, N., Hofmann, R., Alpak, F.O., Berg, S., Dietderich, J., Agarwal, U., Tandon, K., Hunter, S., Freeman, J. & Wilson, O.B., 2017a. References and benchmarks for pore-scale flow simulated using micro-CT images of porous media and digital rocks, Advances in Water Resources, 109, 211-235, doi: 10.1016/j.advwatres.2017.09.007.

Saxena, N., Hofmann, R., Alpak, F.O., Dietderich, J., Hunter, S. & Day-Stirrat, R.J., 2017b. Effect of image segmentation & voxel size on micro-CT computed effective transport & elastic properties, Marine and Petroleum Geology, 86, 972-990, doi: 10.1016/j.marpetgeo.2017.07.004.

Saxena, N., Hows, A., Hofmann, R., Alpak, F.O., Dietderich, J., Appel, M., Freeman, J. & De Jong, H., 2019a. Rock properties from micro-CT images: Digital rock transforms for resolution, pore volume, and field of view, Advances in Water Resources, 134, 103419, doi: 10.1016/j.advwatres.2019.103419.

Saxena, N., Hows, A., Hofmann, R., Alpak, F.O., Freeman, J., Hunter, S. & Appel, M., 2018. Imaging and computational considerations for image computed permeability: Operating envelope of Digital Rock Physics, Advances in Water Resources, 116, 127-144, doi: 10.1016/j.advwatres.2018.04.001.

Saxena, N., Hows, A., Hofmann, R., Freeman, J. & Appel, M., 2019b. Estimating Pore Volume of Rocks from Pore-Scale Imaging, Transport in Porous Media, 129, 403-412, doi: 10.1007/s11242-019-01295-x.

Schindelin, J., Arganda-Carreras, I., Frise, E., Kaynig, V., Longair, M., Pietzsch, T., Preibisch, S., Rueden, C., Saalfeld, S., Schmid, B., Tinevez, J.-Y., White, D.J., Hartenstein, V., Eliceiri, K., Tomancak, P. & Cardona, A., 2012. Fiji: an open-source platform for biological-image analysis, Nature Methods, 9, 676-682, doi: 10.1038/nmeth.2019.

Schlüter, S., Sheppard, A., Brown, K. & Wildenschild, D., 2014. Image processing of multiphase images obtained via X-ray microtomography: A review, Water Resources Research, 50, 3615-3639, doi: 10.1002/2014WR015256.

Shah, S.M., Gray, F., Crawshaw, J.P. & Boek, E.S., 2016. Micro-computed tomography pore-scale study of flow in porous media: Effect of voxel resolution, Advances in Water Resources, 95, 276-287, doi: 10.1016/j.advwatres.2015.07.012.

Shearing, P., Turner, M., Sinclair, I., Lee, P., Ahmed, F., Quinn, P., Leach, R., Sun, W. & Warnett, J., 2018. EPSRC X-Ray Tomography Roadmap 2018, https://epsrc.ukri.org/files/research/epsrc-x-ray-tomography-roadmap-2018/ (accessed 02.10.2019).

Simpleware, 2019. Simpleware ScanIP Technical Data Sheet. Synopsys. https://www.synopsys.com/simpleware/resources/datasheets.html (accessed 02.10.2019).

Soulaine, C., Gjetvaj, F., Garing, C., Roman, S., Russian, A., Gouze, P. & Tchelepi, H.A., 2016. The Impact of Sub-Resolution Porosity of X-ray Microtomography Images on the Permeability, Transport in Porous Media, 113, 227-243, doi: 10.1007/s11242-016-0690-2.

Swanson, B.F., 2013. A Simple Correlation Between Permeabilities and Mercury Capillary Pressures, Journal of Petroleum Technology, 33, 2498-2504, doi: 10.2118/8234-pa.

Tafforeau, P., Boistel, R., Boller, E., Bravin, A., Brunet, M., Chaimanee, Y., Cloetens, P., Feist, M., Hoszowska, J., Jaeger, J.J., Kay, R.F., Lazzari, V., Marivaux, L., Nel, A., Nemoz, C., Thibault, X., Vignaud, P. & Zabler, S., 2006. Applications of X-ray synchrotron microtomography for non-destructive 3D studies of paleontological specimens, Applied Physics a-Materials Science & Processing, 83, 195-202, doi: 10.1007/s00339-006-3507-2.

Tanikawa, W. & Shimamoto, T., 2009. Comparison of Klinkenberg-corrected gas permeability and water permeability in sedimentary rocks, International Journal of Rock Mechanics and Mining Sciences, 46, 229-238, doi: 10.1016/j.ijrmms.2008.03.004.

Van Dalen, G. & Koster, M., 2012. 2D & 3D particle size analysis of micro-CT images, Bruker-microCT User Meeting. Brussels, 2012. 157-171

Vigorito, M. & Hurst, A., 2010. Regional sand injectite architecture as a record of pore-pressure evolution and sand redistribution in the shallow crust: insights from the Panoche Giant Injection Complex, California, Journal of the Geological Society, 167, 889-904, doi: 10.1144/0016-76492010-004.

Vogel, H.J., Tölke, J., Schulz, V.P., Krafczyk, M. & Roth, K., 2005. Comparison of a Lattice-Boltzmann Model, a Full-Morphology Model, and a Pore Network Model for Determining Capillary Pressure–Saturation Relationships, Vadose Zone Journal, 4, 380, doi: 10.2136/vzj2004.0114.

Wildenschild, D. & Sheppard, A.P., 2013. X-ray imaging and analysis techniques for quantifying pore-scale structure and processes in subsurface porous medium systems, Advances in Water Resources, 51, 217-246, doi: 10.1016/j.advwatres.2012.07.018.

Worden, R. & Burley, S., 2003. Sandstone diagenesis: the evolution of sand to stone, Sandstone Diagenesis: Recent and Ancient, 4, 3-44, doi: 10.1002/9781444304459.ch.

Wu, F., Hurst, A. & Grippa, A., 2017. Grain and pore microtexture in sandstone sill and depositional sandstone reservoirs: preliminary insights, Petroleum Geoscience, doi: 10.1144/petgeo2017-027.

Youssef, S., Rosenberg, E., Gland, N., Skalinski, M. & Vizika, O., 2007. High Resolution CT and Pore-Network Models to Assess Petrophysical Properties of Homogeneous and Heterogeneous Carbonates, Society of Petroleum Engineers, 1-12, doi: 10.2118/111427-MS.

Zahasky, C., Jackson, S.J., Lin, Q. & Krevor, S., 2020. Pore network model predictions of Darcy-scale multiphase flow heterogeneity validated by experiments, Water Resources Research, doi: 10.1029/2019WR026708.

Zhang, S., Klimentidis, R.E. & Barthelemy, P., 2011. Porosity and permeability analysis on nanoscale FIB-SEM 3D imaging of shale rock. International Symposium of the Society of Core Analysts, pp. 18-21, SCA2011-30.

Zhang, S., Klimentidis, R.E. & Barthelemy, P., 2012. Micron to millimeter upscaling of shale rock properties based on 3D imaging and modeling. International Symposium of the Society of Core Analysts, pp. 30, SCA2012-20.

Zhu, W., Gaetani, G.A., Fusseis, F., Montesi, L.G.J. & De Carlo, F., 2011. Microtomography of Partially Molten Rocks: Three-Dimensional Melt Distribution in Mantle Peridotite, Science, 332, 88-91, doi: 10.1126/science.1202221.

Tables

Table 1. Image dimensions, resolution, grain size, pore throat size and porosity values of samples St1-2 and A-C used for XCT image analysis.

Sample no.	Image Resolution (µm)	Max. dimensions (Voxels)	Max. Length (mm)	D_{eff} (µm)	D_d (µm)	ϕ_t (%)	ϕ_c (%)
St1	5	1000	5.00	190	34	11.66	11.32
St2	3.5	788	2.76	350	n/a	34.34	34.33
A	0.81	1728	1.40	140	24	15.70	15.31
A2	0.81	1728	1.40	140	24	15.14	14.83
B	0.81	1728	1.40	140	27	13.69	13.43
C	0.81	1728	1.40	140	23	9.58	8.32

Cubic volumes were used in this study. $\phi\tau$ and $\phi\chi$ are total porosity and connected porosity, respectively. D_{eff} and D_d are average grain and pore throat diameters, respectively.

Table 2. Results of permeability calculated from 27 XCT image sub-volumes of samples A-C and eight sub-volumes of sample St1, used to further understand the REV (representative elementary volume) size of each sample.

Sample	No. of sub-vol.	Sub-Vol. (voxels)	Sub-Vol. (mm^3)	min. k_h (mD)	max. k_h (mD)	int. k_h (mD)	min. k_v (mD)	max. k_v (mD)	int. k_v (mD)
A	27	576^3	0.47^3	4	1414	262	25	760	306
B	27	576^3	0.47^3	5	651	184	3	1137	385
C	27	576^3	0.47^3	0	178	25	0	296	31
St1	8	400^3	2.5^3	235	467	423	164	511	416

Sub-Vol, sub-volume; min. and max., minimum and maximum; k_h and k_v, permeability in the horizontal and vertical directions; int. k_h and int. k_v, interpolated values of permeability calculated from the porosity-permeability plots displayed in Figure 11.

Table 3. Results of upscaled permeability calculated from 27 XCT image sub-volumes of samples A, B, C and eight sub-volumes of sample St1 using Matlab Reservoir Simulation Toolbox (MRST). Volume averaged calculations of the arithmetic, harmonic and harmonic-arithmetic means are determined.

Sample	No. of sub-vol.	Sub-Vol. (voxels)	Sub-Vol. (mm^3)	Ar. k_h (mD)	H.-Ar. k_h (mD)	H. k_h (mD)	A. k_v (mD)	H.-Ar. k_v (mD)	H. k_v (mD)
A	27	576^3	0.47^3	248	103	42	294	208	136
B	27	576^3	0.47^3	181	83	31	379	227	39
C	27	576^3	0.47^3	22	6	0	28	7	0
St1	8	400^3	2.5^3	235	467	423	164	511	416

Sub-Vol, sub-volume; Ar., Arithmetic mean; H.-Ar., Harmonic-Arithmetic meam; H., Harmonic mean; k_h and k_v, permeability in the horizontal and vertical directions.

Table 4. Laboratory experimental results of porosity calculated by He-pycnometry, as well as results of permeability calculated from a helium flow through-test at 800 kPa confining pressure.

Sample	St1 (Berea)	A	B	C
Cementation	Minor	Uncemented	Uncemented	Silica
ϕ_t (%)	19.8	29.9	23.8	27.9
std.	n/a	0.068	0.163	0.078
k_v (mD)	275	83	25	50
std.	n/a	3.924	1.549	3.363

ϕ_t is total porosity, k_v is permeability in the vertical direction, and std. are the standard deviation values of the porosity and permeability measurements. Each permeability experiment was repeated three times.

Table 5. Results of porosity and permeability, which have been calculated for the XCT image volumes following downsampling / numerically coarsening by a factor of 1-8 post-segmentation.

Sample	N.C. Fac.	Image Res. (μm)	Volume (voxels)	Volume (mm^3)	ϕ_t (%)	ϕ_c (%)	k_h (mD)	k_v (mD)	Time (minutes)
A	1	0.81	1728^3	1.4^3	15.70	15.31	n/a	n/a	n/a
	2	1.62	864^3	1.4^3	14.68	14.22	n/a	n/a	n/a
	3	2.43	576^3	1.4^3	15.56	14.95	290	355	60
	4	3.24	432^3	1.4^3	14.70	13.88	279	335	20
	6	4.86	288^3	1.4^3	14.35	13.29	286	348	5
	8	6.48	216^3	1.4^3	13.87	12.43	279	350	3
B	1	0.81	1728^3	1.4^3	13.69	13.43	n/a	n/a	n/a
	2	1.62	864^3	1.4^3	12.69	12.39	n/a	n/a	n/a
	3	2.43	576^3	1.4^3	13.56	13.16	355	479	60
	4	3.24	432^3	1.4^3	12.76	12.10	341	461	20
	6	4.86	288^3	1.4^3	12.48	11.50	351	503	5
	8	6.48	216^3	1.4^3	12.01	10.73	318	530	3
C	1	0.81	1728^3	1.4^3	9.58	8.32	n/a	n/a	n/a
	2	1.62	864^3	1.4^3	8.46	6.95	n/a	n/a	n/a
	3	2.43	576^3	1.4^3	9.33	7.17	78	57	60
	4	3.24	432^3	1.4^3	8.35	5.50	67	46	20
	6	4.86	288^3	1.4^3	7.84	4.52	67	38	5
	8	6.48	216^3	1.4^3	7.16	3.45	61	25	3

N.C. fac. is the numerical coarsening / downsampling factor applied to the XCT images post-segmentation. Post-segmentation refers to XCT images which have already been segmented at 1 μm (0.81 μm) image resolution. ϕ_t and ϕ_c are total porosity and connected porosity respectively, k_h and k_v are permeability in the horizontal and vertical directions. Image Res. is image resolution. Values described as n/a were not computable as they exceed computational memory limits.

Table 6. Results of porosity and permeability for the XCT images if the clay mineral fraction and cement matrix are re-assigned to the pore phase, compared with the experimentally derived results.

Sample	A	B	C
Cementation	Uncemented	Uncemented	Silica
ϕ_t - Pore phase + clay fraction & cement matrix (%)	28.97	23.10	27.11
k_v - Pore phase+ clay fraction & cement matrix (mD)	2352	2415	1345
ϕ_t - Core experiment (%)	29.88	23.75	27.90
k_v - Core experiment (mD)	83	25	50

ϕ_t and k_v are total porosity and vertical permeability respectively. The top two rows show the output values of porosity and permeability when the XCT images are re-segmented to include the clay mineral fraction and cement matrix. The bottom two rows show the experimentally derived values, previously shown in Table 3.

Table 7. Results summary of calculated porosity and permeability, showing the comparison of the XCT image-based calculations and laboratory measurements, [2] vs [3] and [5-8] vs [9]. For samples A-C, XCT permeability and porosity calculations can be acheived within one order of magnitude and porosity values <1 % of laboratory physical measurements. Image based methods [5-8a] show strong agreement.

Sample	A	B	C	St1
Cementation	Uncemented	Uncemented	Silica	Minor
[1] ϕ_t - Pore Phase (%)	15.7	13.69	9.58	11.66
[2] ϕ_t - Pore phase + clay fraction & cement matrix (%)	28.97	23.10	27.11	15.82
[3] ϕ_t - Core experiment (%)	29.88	23.75	27.90	19.82
[4] k_v - One sub-volume (mD)	275 [25-760]	185 [3-1137]	1 [0-296]	448 [164-511]
[5] k_v - Maximum sample volume with NC Factor of 3 (mD)	355	479	57	n/a
[6] k_v - Maximum sample volume with PNM (mD)	291	500	23	235
[7] k_v – Interpolated from multiple sub-volumes (mD)	306	385	31	416
[8a] k_v – MRST Upscaling – Arithmetic mean (mD)	294	379	28	393
[8b] k_v – MRST Upscaling – Harmonic-arithmetic mean (mD)	208	227	7	379
[8c] k_v – MRST Upscaling – Harmonic mean (mD)	136	39	< 1	350
[9] k_v - Core experiment (mD)	83	25	50	275

ϕ_t and k_v are total porosity and vertical permeability respectively. Described for clarity: [1] is the total porosity of the air phase calculated from the maximum XCT image volumes shown in Table 1. [2] is the total porosity of the pore phase calculated from re-segmentation of the XCT images to include the clay mineral fraction and cement matrix. [3] is the total porosity of the pore phase calculated from the laboratory experiments. [4] is the vertical permeability calculated from one subvolume of each XCT image. The permeability range is shown in square brackets, calculated from 27 sub-volumes, as shown in Table 2. [5] is the vertical permeability calculated from the maximum XCT image volumes using numerical coarsening. To compute permeability of the maximum XCT image volume size, the XCT image was downsampled post-segmentation by a numerical coarsening (NC) factor of 3, as shown in Table 4. [6] Is the vertical permeability calculated from the maximum XCT image volume using pore network modelling (PNM). [7] is the interpolated vertical permeability value calculated from multiple subvolumes, as shown in Table 2. [8] is the upscaled vertical permeability calculated and modelled using the MATLAB reservoir simulation toolbox (MRST), derived from a cartesian grid of the multiple subvolumes. The arithmetic [8a], harmonic-arithmetic [8b] and harmonic means [8c] are calculated. [9] is the vertical permeability calculated using physical laboratory measurements, as shown in Table 3.

Figures

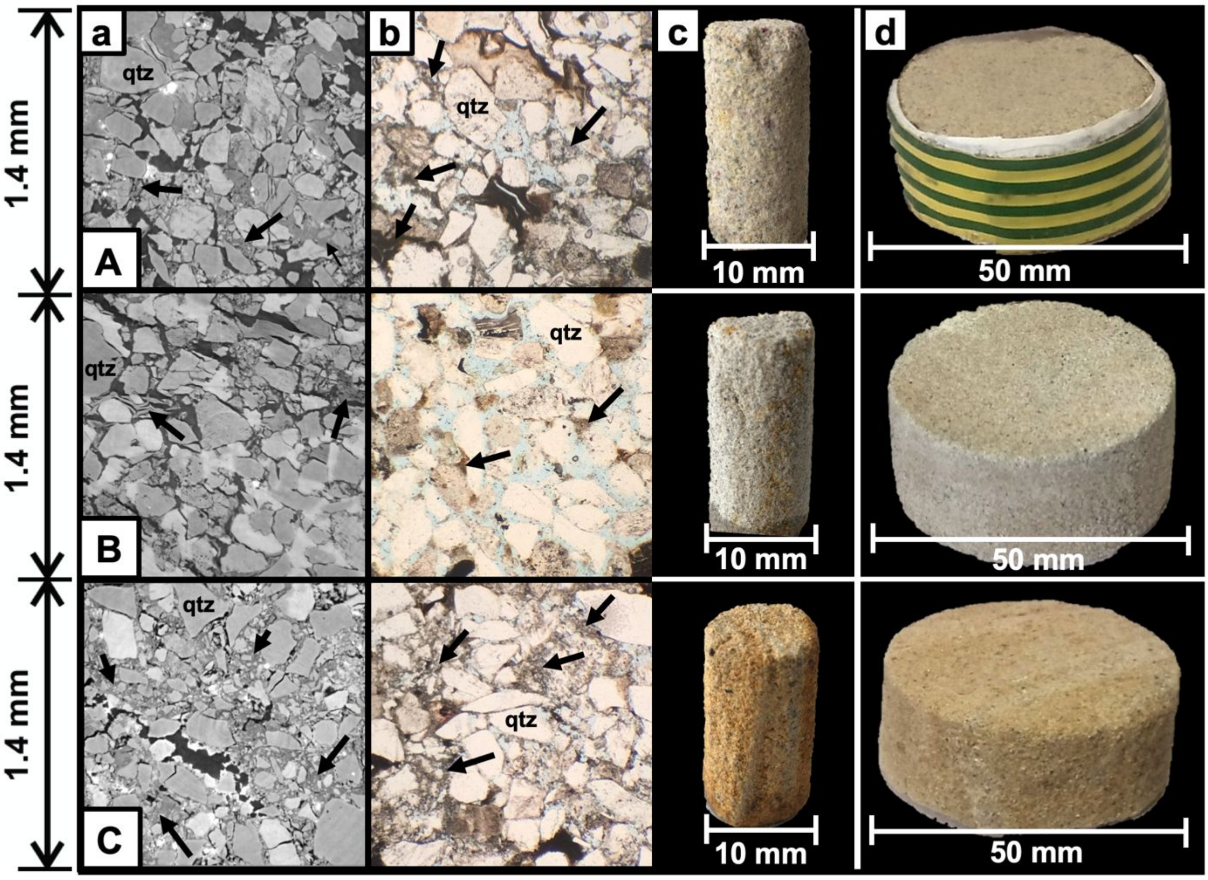

Figure 1. Images of the samples (A,B,C) used in laboratory physical measurements at different scales from left to right: (a) 2D greyscale images in the horizontal plane of the sample sub-volumes, (b) Thin section images indicating predominantly quartz grains (pastel yellow), pore space (light blue), as well as clay minerals and cement matrix (brown-black), (c) The 10 mm diameter samples used for X-ray micro-CT (XCT) image analysis and (d) The 50 mm diameter core plugs used for the laboratory physical measurements**,** cored from the same block as the XCT samples.

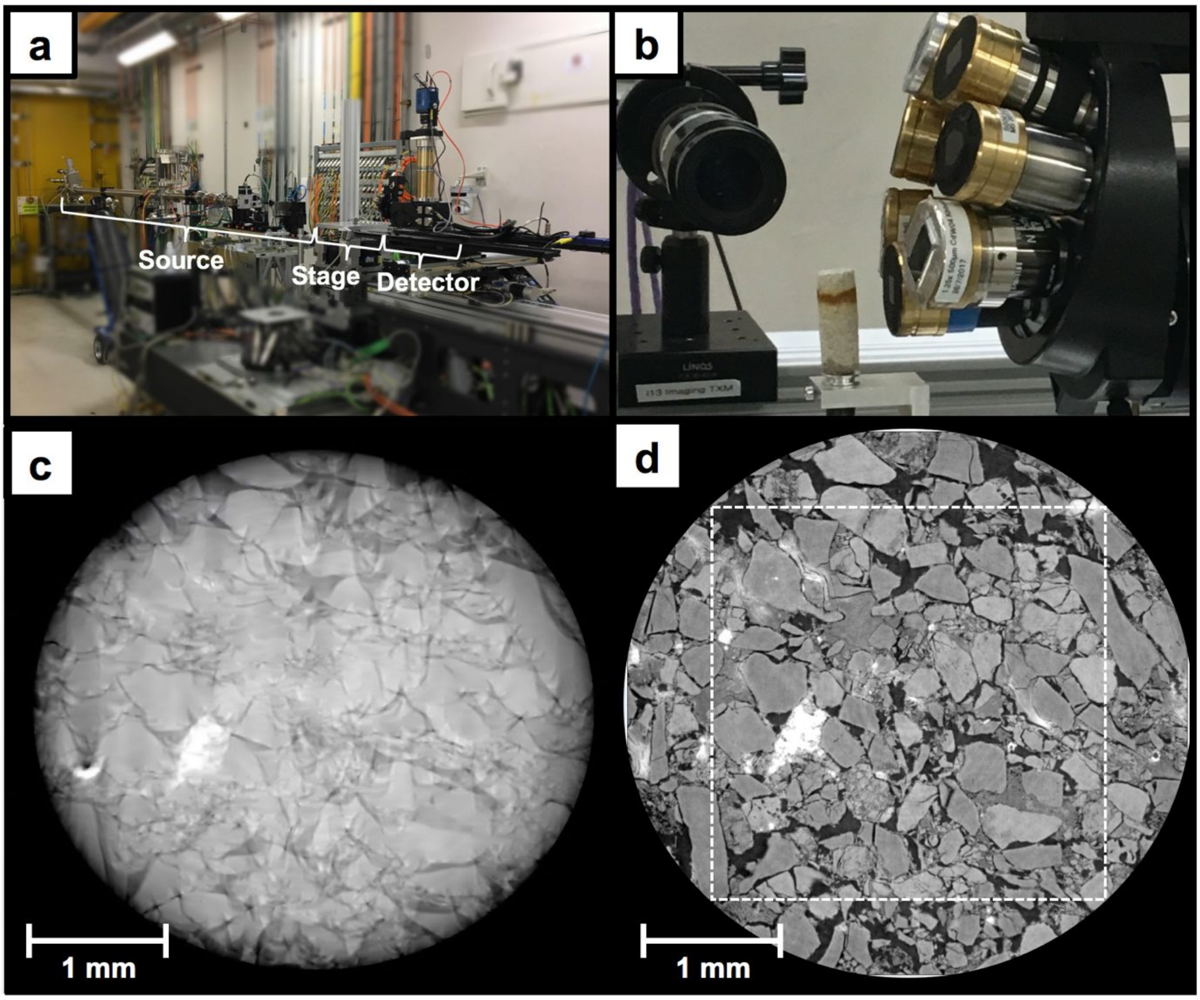

Figure 2. Photographs of the experimental setup at Diamond Synchrotron beamline I13-2. (a) The experimental hall showing the parallel beam source. (b) Sandstone sample mounted to the stage using a SEM stub, placed between the source and a pco.edge 5.5 scintillator-coupled detector with 4x objective lens, providing a 1 µm (0.81 µm) pixel size and 2.1 x 1.8 mm field of view. (c-d) Acquired images reconstructed using Savu with poorly optimised settings (c) and optimal settings (d).

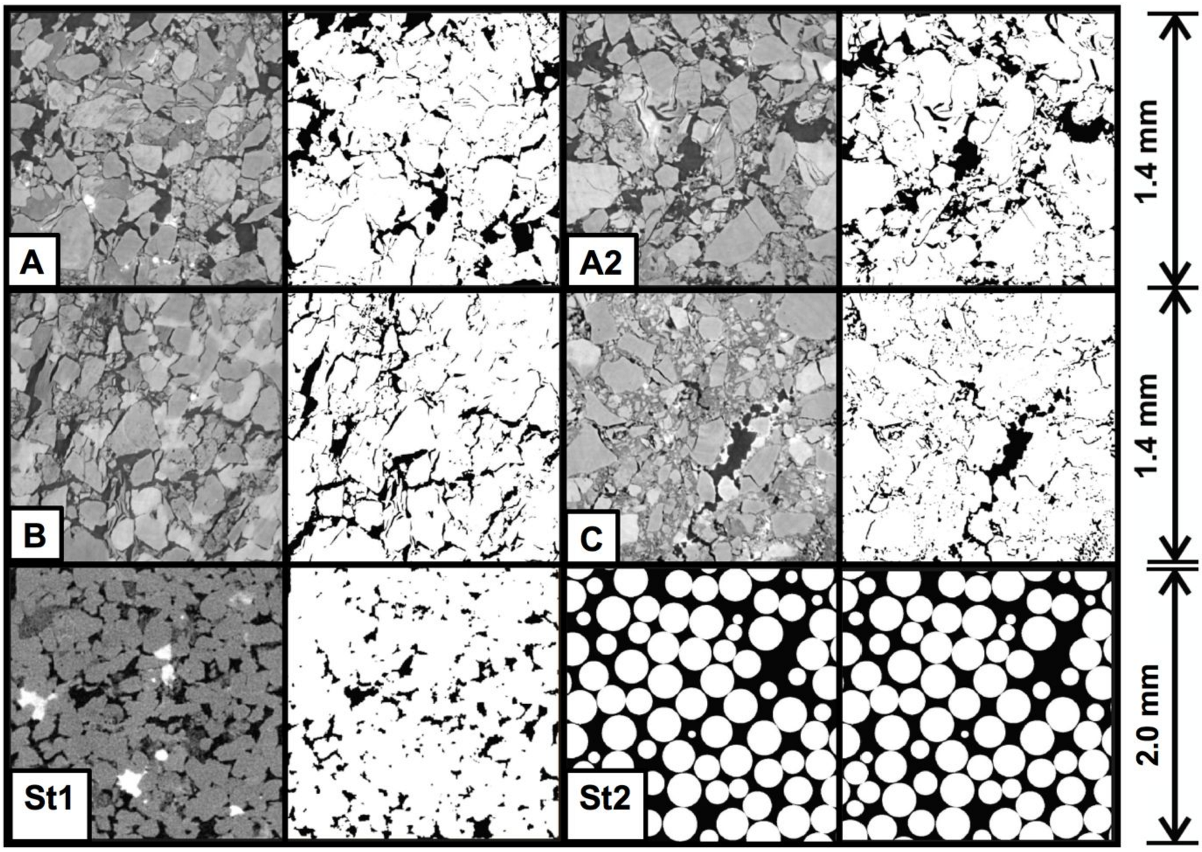

Figure 3. Scanned images and the result of segmentation for samples analysed. 2D orthoslices in the horizontal plane of the sample sub-volumes displaying greyscale images prior to segmentation (left) and binarised images post-segmentation (right). The binarised images display pore space in black and the solid phase in white: (A-C) Heterogeneous sandstone samples which are uncemented (A, A2, B) and silica cemented (C) respectively. Two standards were also used in the study: (St1) Berea sandstone and (St2) a sphere pack (Andra et al. 2013a).

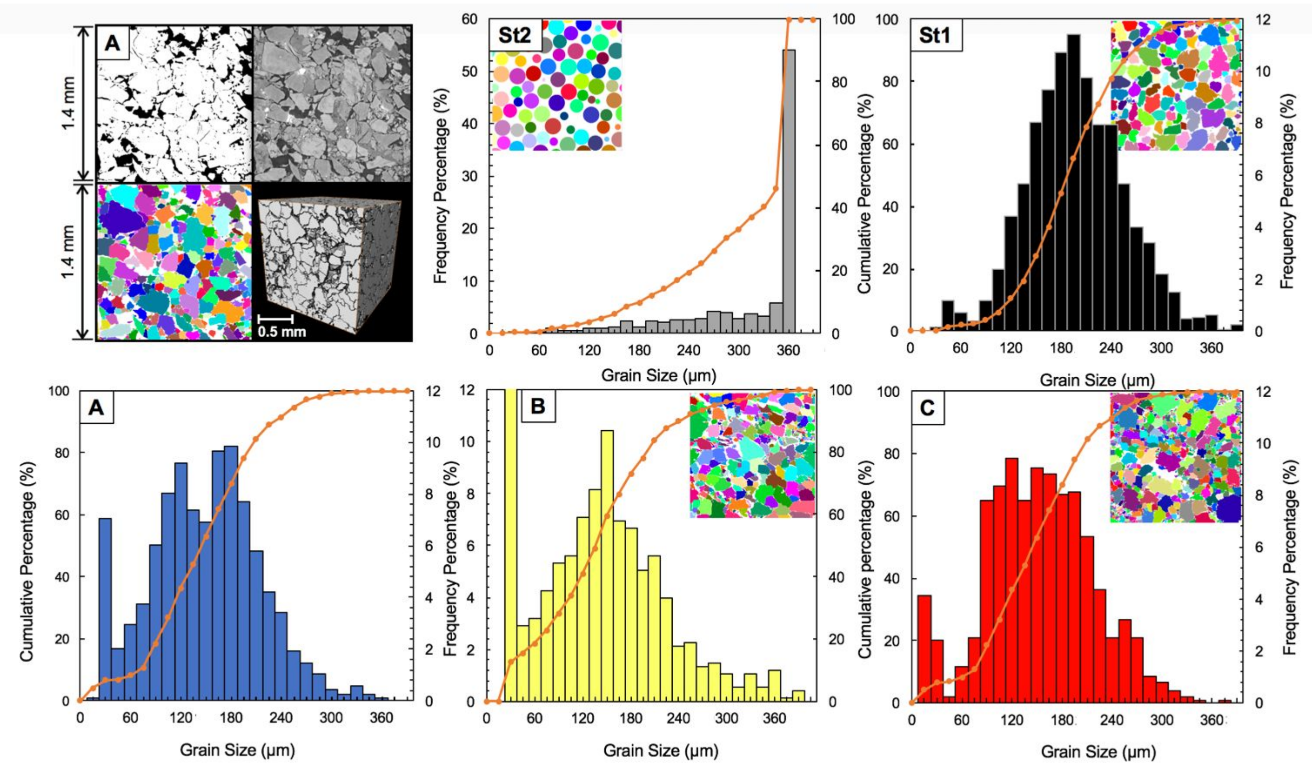

Figure 4. Grain size distribution comparisons of XCT samples for homogeneous standards St1-2 and heterogeneous samples A-C. The frequency histograms are binned into 15 µm intervals. Orange lines show cumulative frequency percentage. The images show the result of the 3D grain size process, implemented using a watershed separation method.

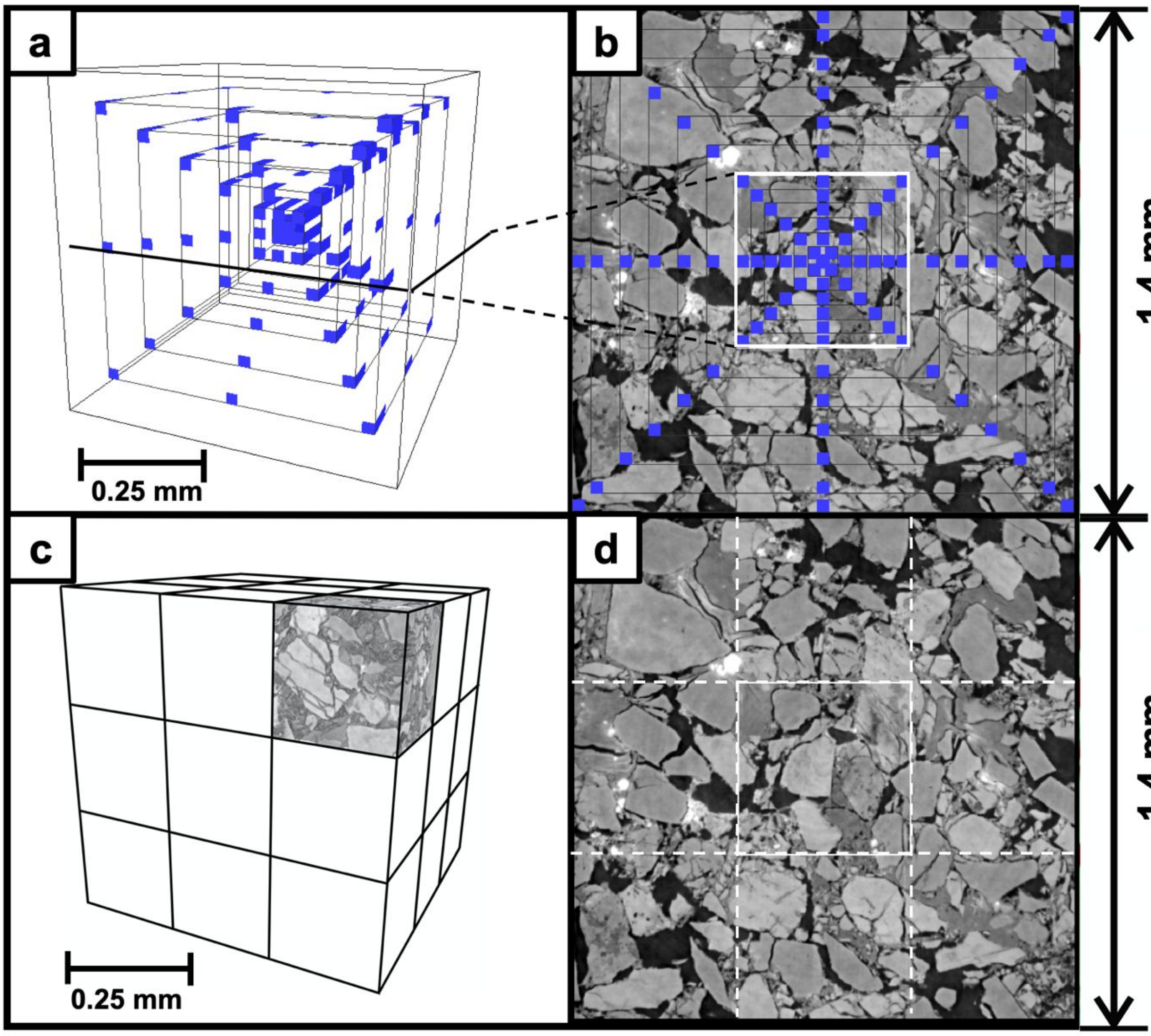

Figure 5. Sample subvolume A, displaying different volume sizes used for the representative volume (REV) study, ranging from 0.04 – 1.40 mm width (equivalent to sample lengths N_{REV} <1 to 10). Two different volume configurations are used for the REV analysis. (a-b) A nested volume sequence, shown by black solid lines with blue squares at the corners and edge centres. (c-d) A cartesian grid of 0.5 mm (N_{REV} = 3.5) subvolumes. 1.40 mm width (N_{REV} = 10) is the maximum sample lengths of A-C.

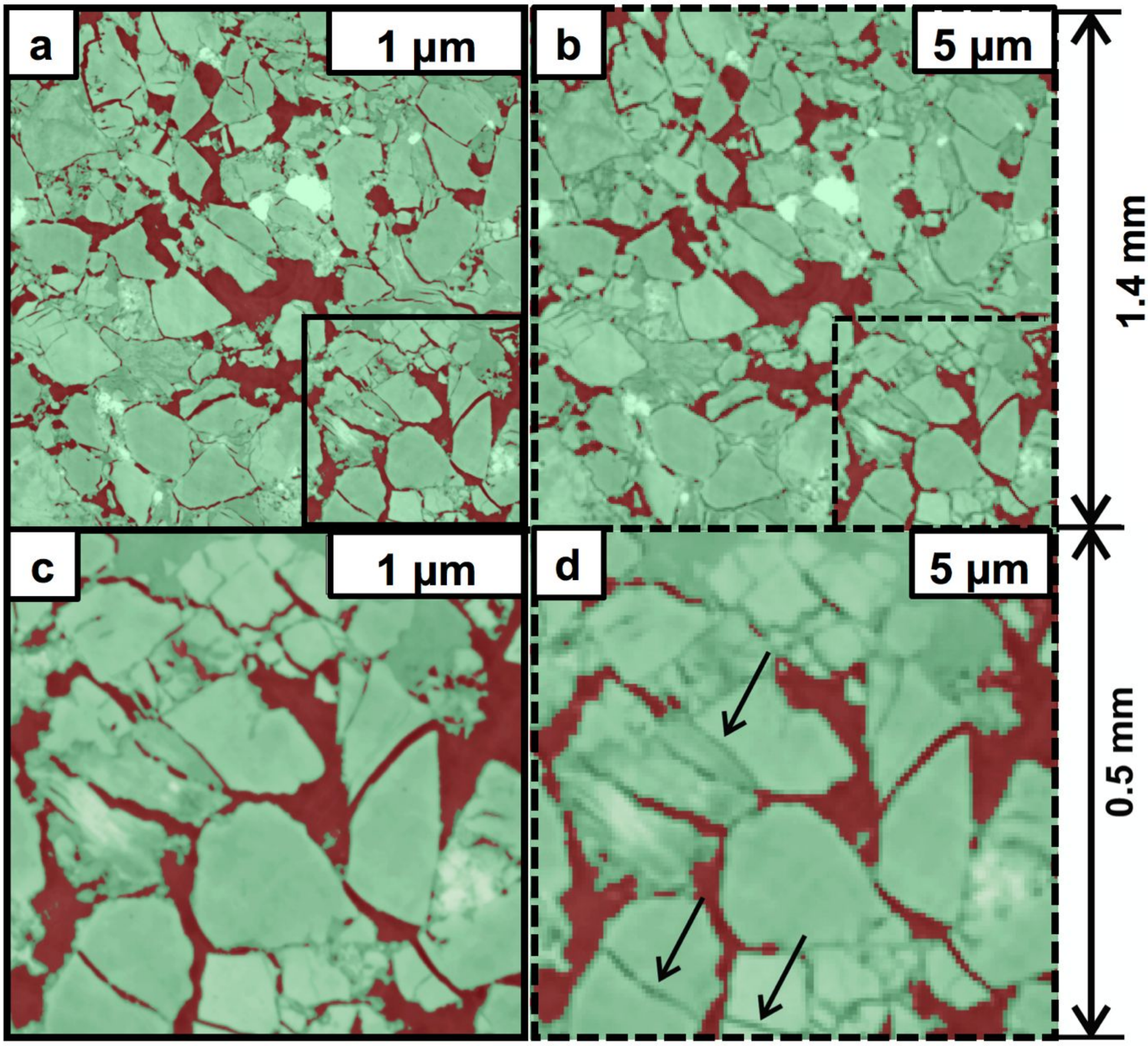

Figure 6. Demonstration of the impact of down-sampling image segmentation in characterising intergranular micro-pores. (a,c) 2D orthoslice of sample A showing the 3D weka segmentation result at the original voxel size of 1 µm (0.81 µm). (b,d) A coarsened / downsampled voxel size of 5 µm (right). Red and green indicates areas classified as pore phase and solid phase respectively. The arrows in (d) indicate small intergranular pores which are unresolved by the segmentation method at 5 µm, and are inaccurately classified to the solid phase.

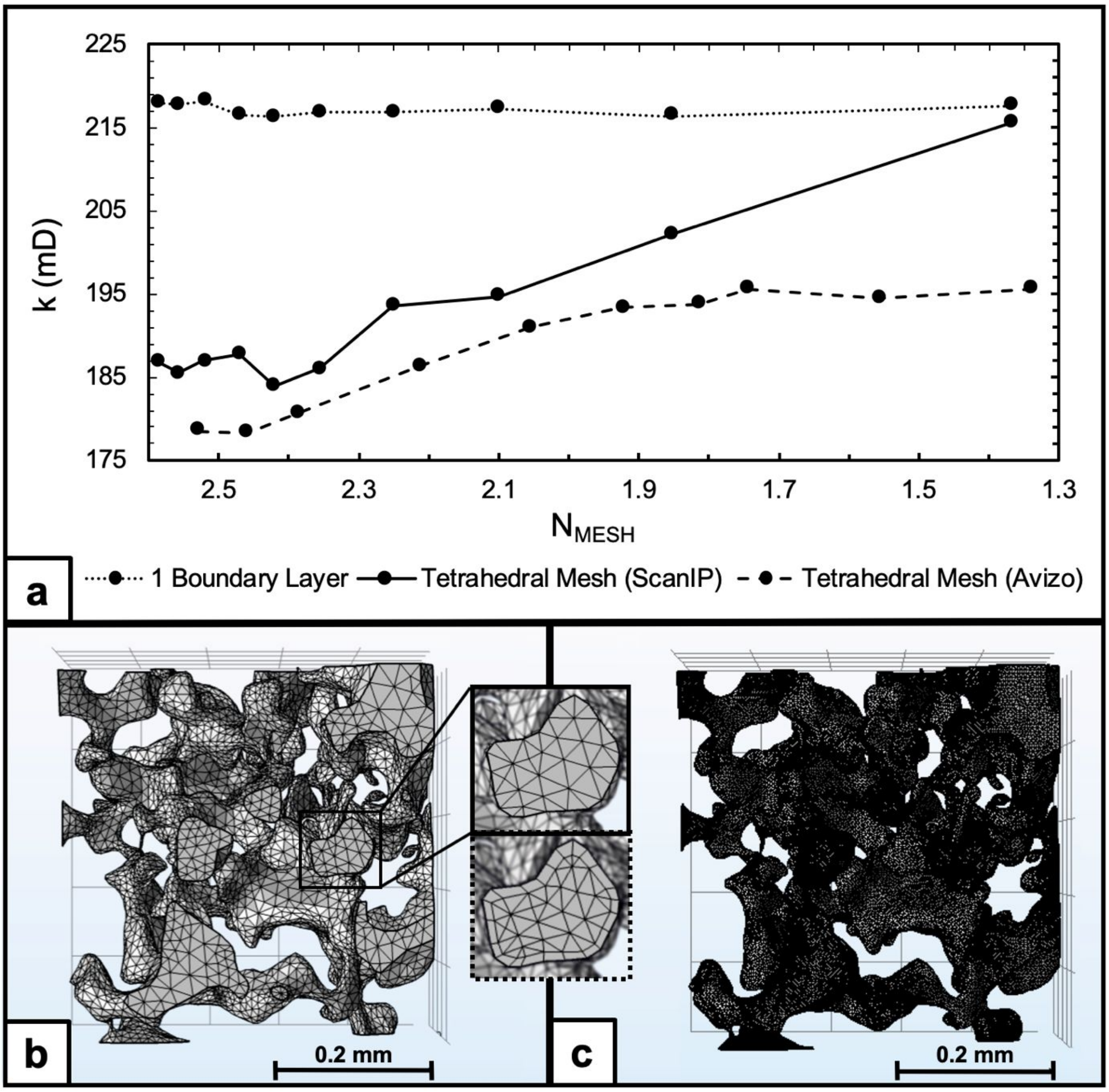

958

959 **Figure 7.** Mesh element study on a 100^3 voxel sub-volume of St1 (Berea Sandstone) showing (a) the

960 change of permeability with increased number of tetrahedral elements. N_{MESH} is a function of mean

961 mesh edge length / image voxel size (Δx), and is not volume size dependent. N_{MESH} ranges from 2.6 to

962 1.35, equivalent to a mean mesh edge length of 13 to 7 µm, or an approximate linear range of (b)

963 50,000 to (c) 350,000 tetrahedral elements. Zoomed in image shows a comparison of a mesh without

964 (solid line) and with (dotted line) a boundary layer. A N_{MESH} value of 2.6 with no boundary layer was

965 used for the fluid simulation comparison analysis.

966

967

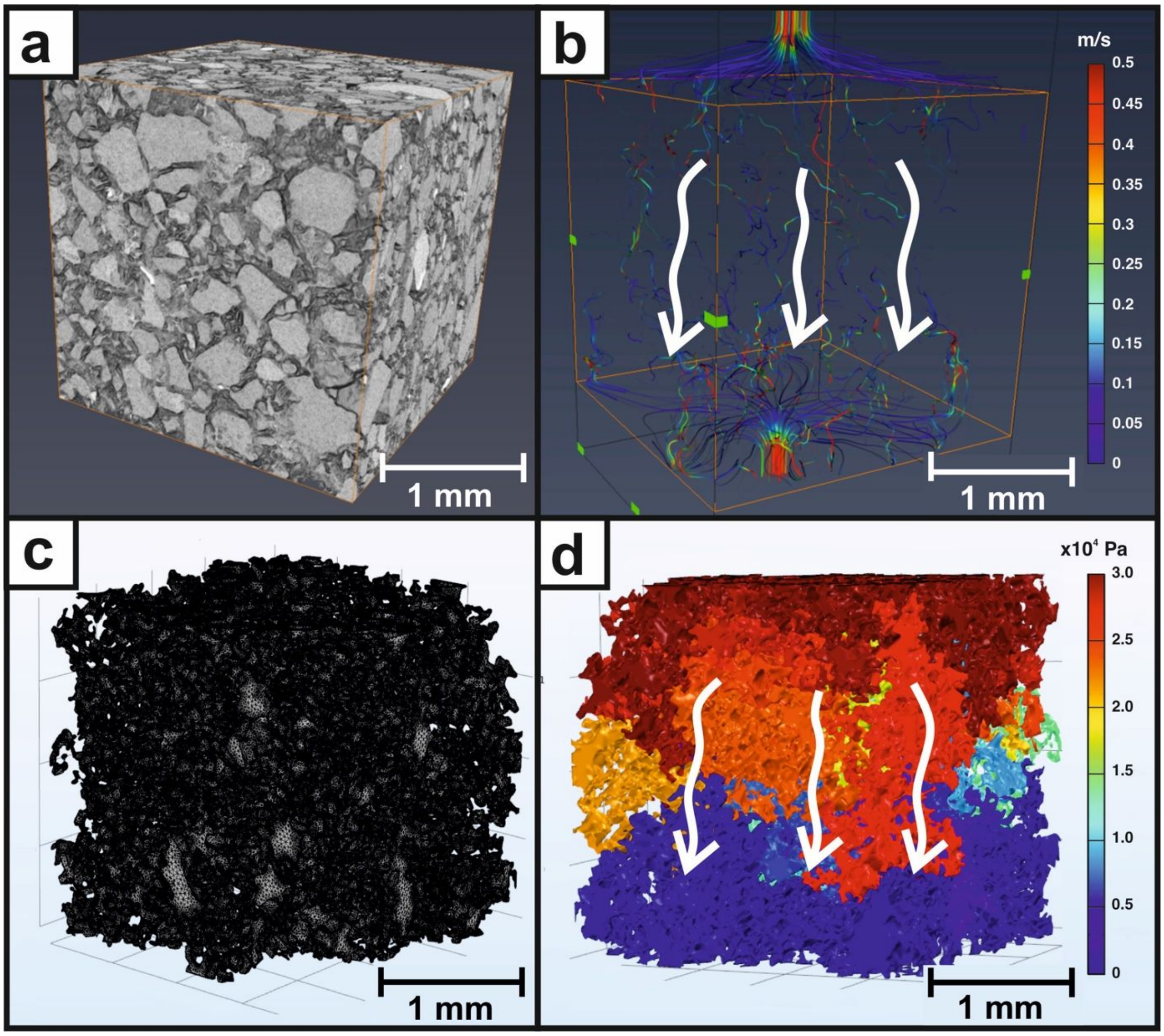

Figure 8. Volume rendering of sample A, showing the two finite element modelling (FEM) Stokes-flow simulation methods used in this study. (a, b) Avizo displaying a (a) 3D greyscale volume and (b) generated fluid velocity profile. Experimental set-ups are added onto sample faces perpendicular to the main flow direction to achieve a quasi-static pressure state. (c, d) Comsol displaying a (c) 3D tetrahedral mesh of the pore phase (N_{MESH} value of 2.6 with no boundary layer) and (d) the pressure gradient profile of the simulation. Colours in (d) represent pressures from 30,000 Pa (dark red) to 0 Pa (dark blue). See supplementary material for video animations.

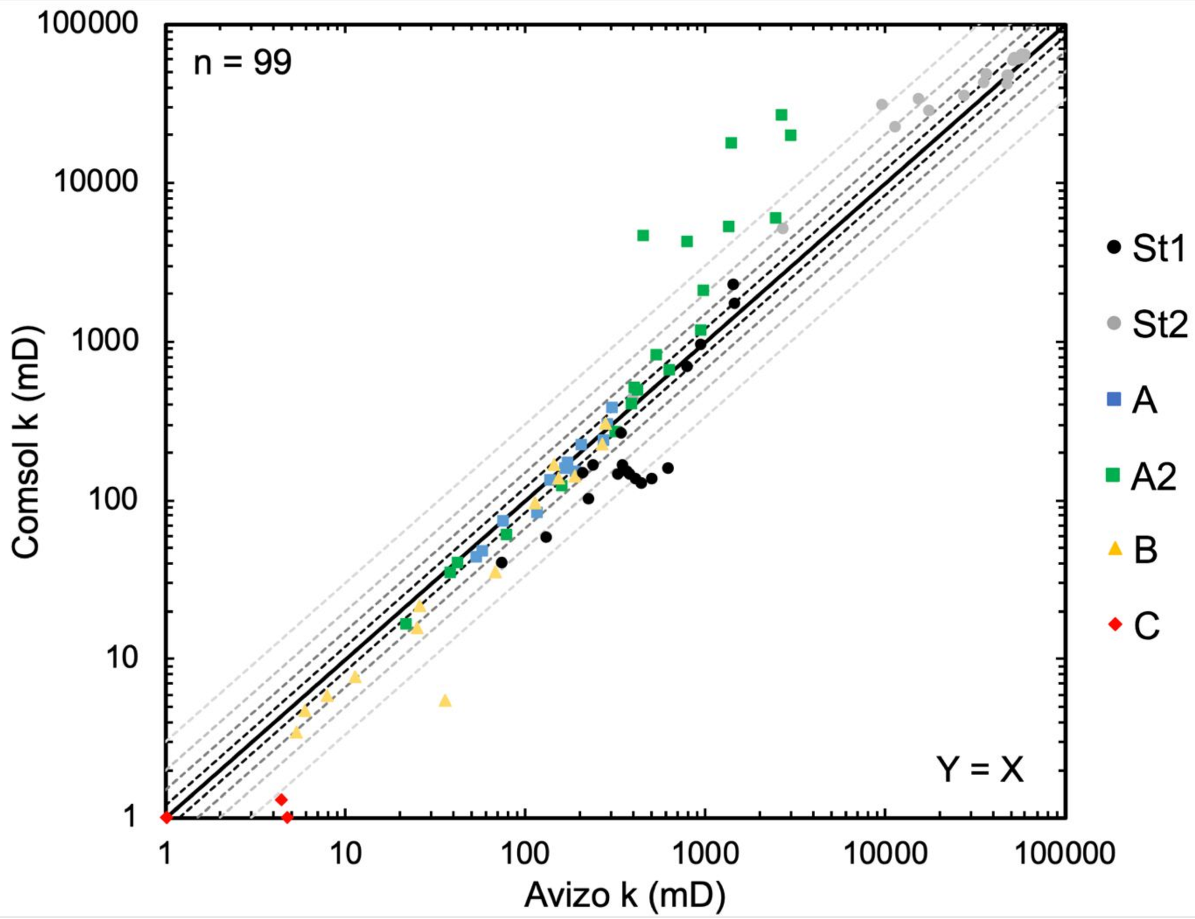

Figure 9. Direct comparison of absolute permeabilities from Avizo and Comsol, the two finite element modelling Stokes-flow simulation methods used in this study. The black solid line indicates the identity line (Y=X) where both methods produce the same permeability. The dashed lines represent uncertainty intervals of 20% (black), 50% (dark grey), 100% (grey) and 200% (light grey). 99 simulations are compared, comprising of samples: St1 (black circle), St2 (grey circle), A (blue square), A2 (green square), B (yellow triangle) and C (red diamond).

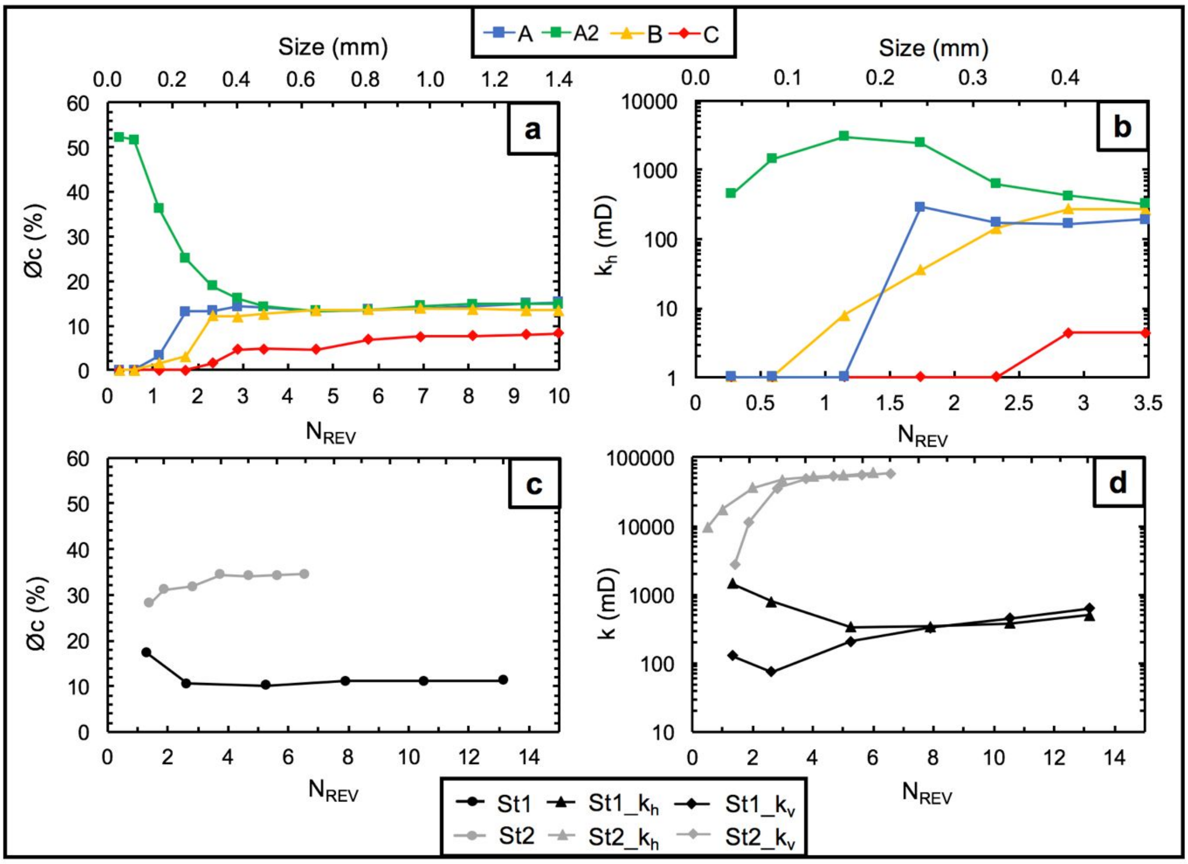

Figure 10. Plots of connected porosity ($Ø_c$) and permeability (k) vs sub-volume size (the cubic length) for samples A-C (a-b) and St1-2 (c-d). The permeability results are from the Avizo Stokes-flow simulation method. N_{REV} is the ratio of sample length to effective grain size, i.e. a N_{REV} value of one is equal to one grain diameter.

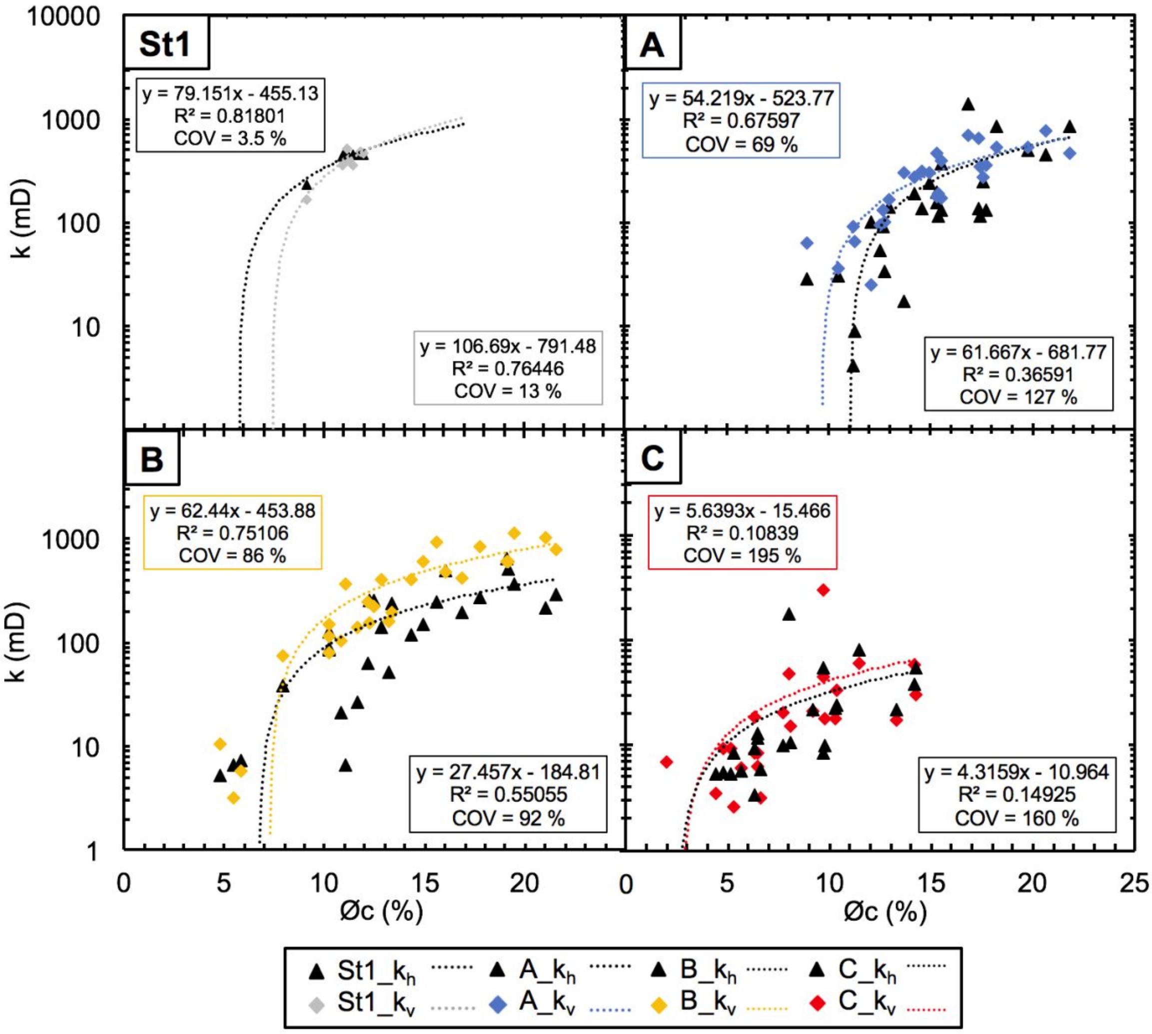

Figure 11. Log-linear plots of permeability (k) against connected porosity ($Ø_c$) for homogeneous samples St1 and heterogeneous samples A, B, and C. St1 shows 8 sub-volumes from the maximum sample volume. A, B and C show 27 sub-volumes from the maximum 1.4 cubic mm sample volume. For each sample, best fit lines for vertical (k_v) and horizontal (k_h) permeabilities are obtained using the known $Ø_c$ from the maximum sample volumes (N_{REV} = 10). COV is the coefficient of variation expressed in percentage (standard deviation/mean).

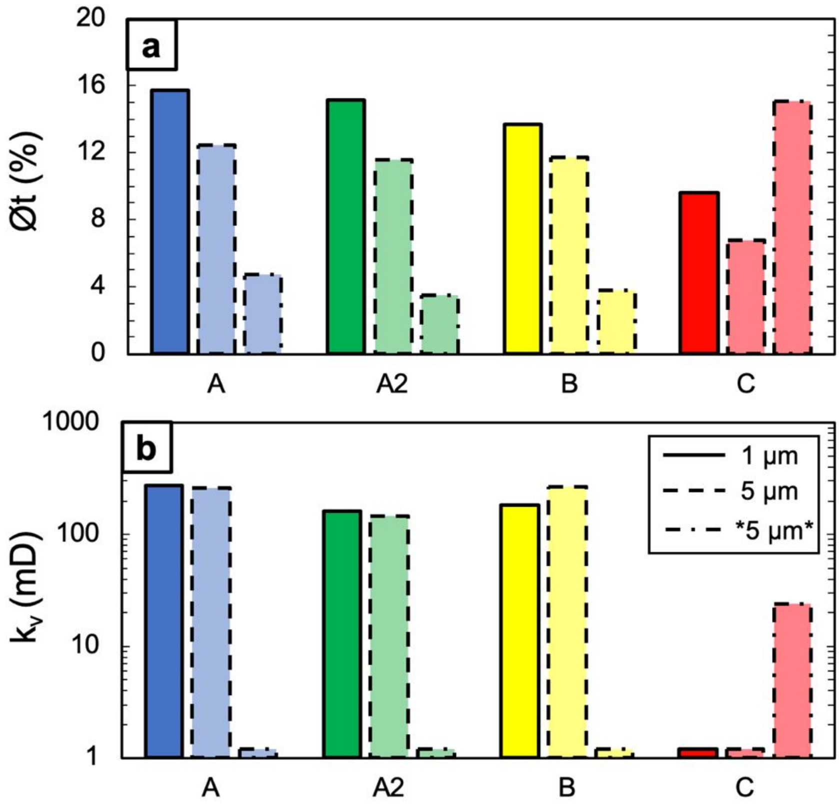

Figure 12. Demonstration of the impact of down-sampling image resolution on porosity-permeability. Comparison of (a) total porosity ($Ø_t$) and (b) vertical permeability (k_v) for original (1 µm) and downsampled (5 µm) images for samples: A (blue), A2 (green), B (yellow) and C (red). Sample sub-volumes of 1.4 mm and 0.5 mm cubic length (N_{REV} = 10 and 3.5) are used for calculations in a) and b), respectively. Original images – straight lines; downsampled images segmented using a classifier trained with the 5 µm images– dashed lines and 1 µm images – dot-dashed lines, respectively.

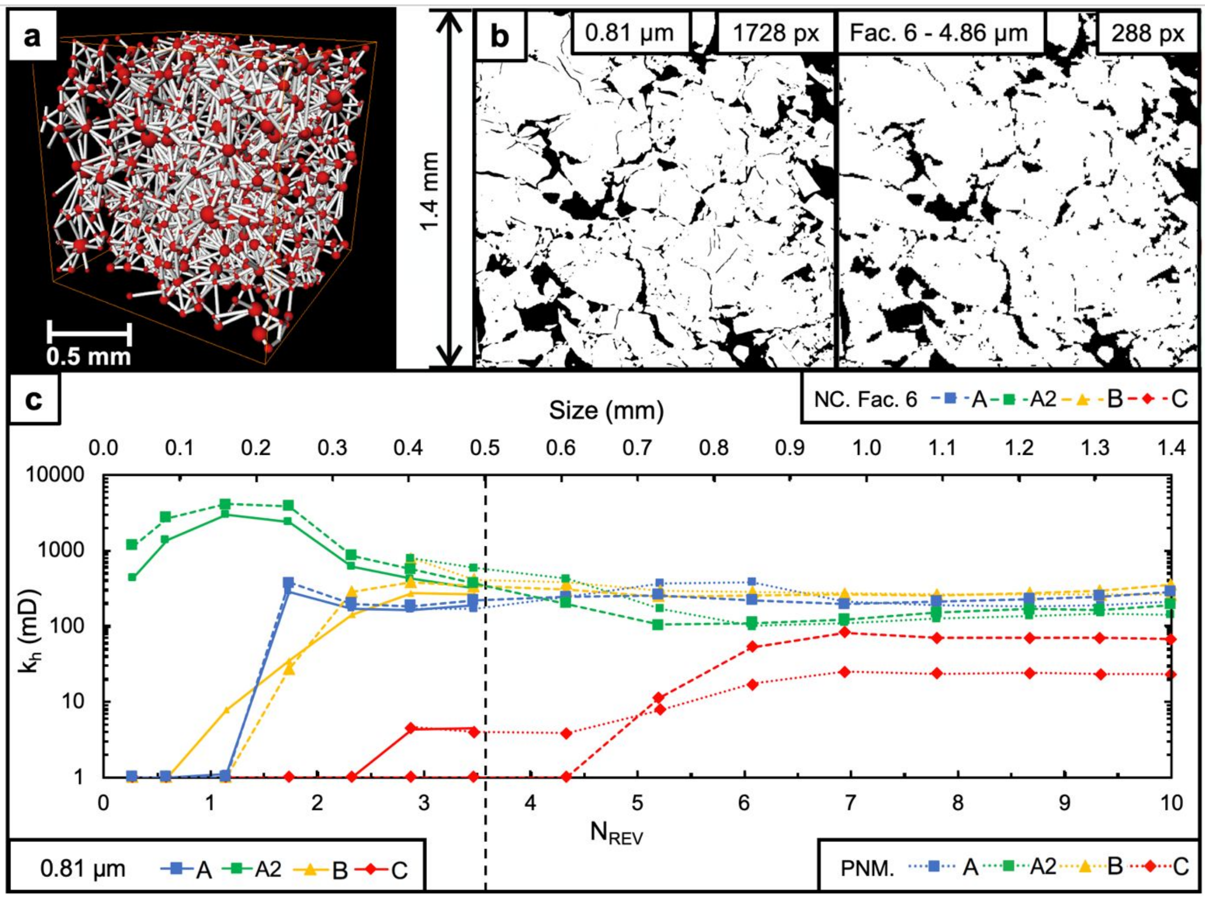

Figure 13. Determination of sample representative elementary volume (REV) using Pore network modelling and Numerical Coarsening of the image (downsampling post-segmentation). (a) Pore network model (PNM) of sample A. Pores – red spheres; pore throats – white sticks. (b) 2D binarised orthoslices of sample A coarsened by a factor (NC. Fac.) of 6. Pore phase – black; solid phase - white. (c) Plot of horizontal permeability (kh) vs sub-volume size (the cubic length) for samples: A (blue square), A2 (green square), B (yellow triangle) and C (red diamond). REV is determined as $N_{REV} \geq 7$ for all samples. NC. Fac. 6 – dashed line; PNM. – dotted line; 0.81µm – solid line. Vertical black dashed line represents the maximum sample size ($N_{REV} = 3.5$) that can be calculated at an image resolution of 0.81 µm within current computational constraints, see Figure 10.

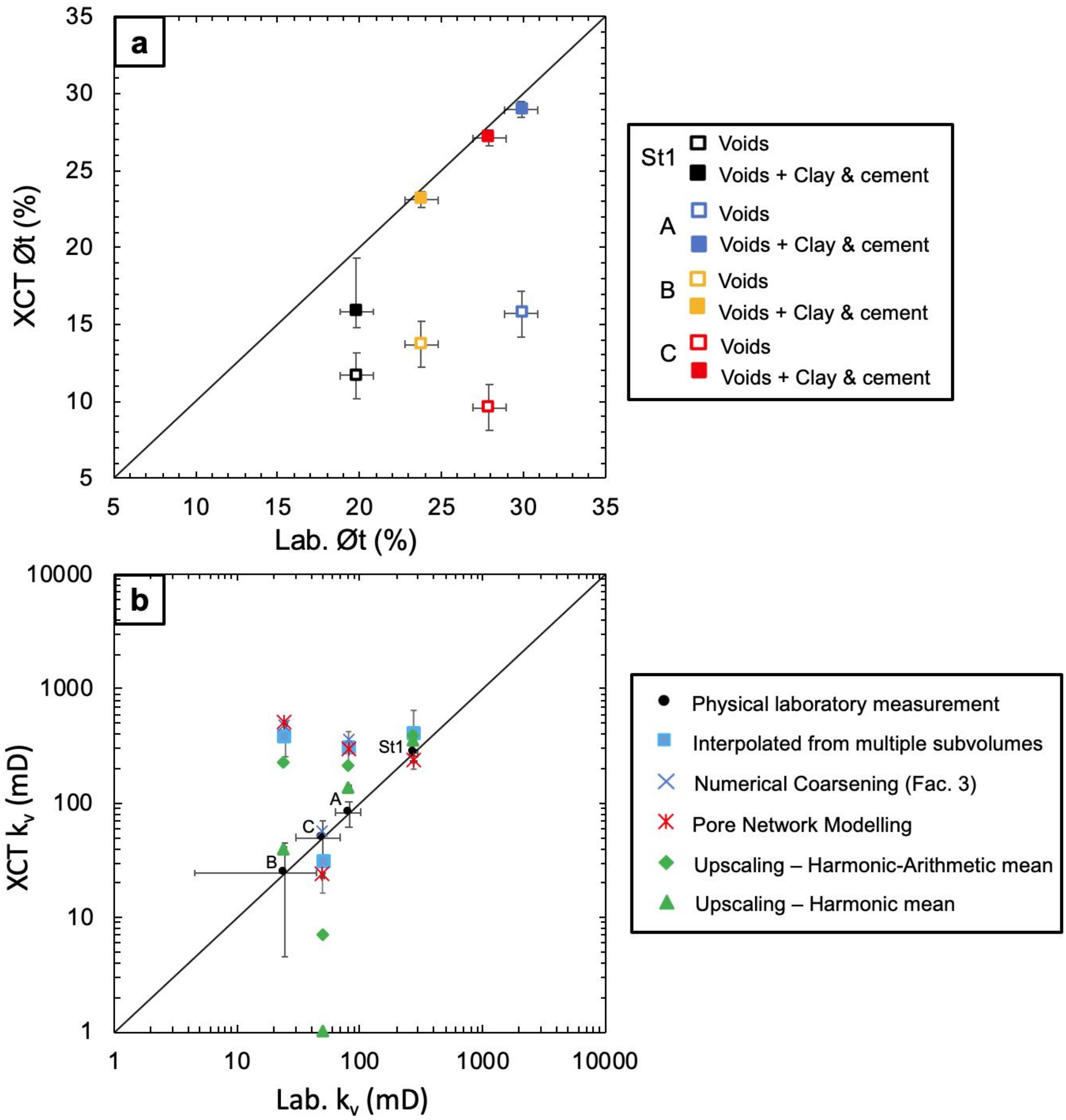

Figure 14. Comparison plots of total porosity (øt) and vertical permeability (k_v) comparing calculations obtained from X-ray micro-CT (XCT) image-based methods and laboratory physical measurements (Lab.). The horizontal (and vertical) error bars for the laboratory data in both plots correspond to the standard deviation of the repeated physical measurements. (a) For the XCT data points, øt is calculated for voxels classified to voids only (white markers), and voxels classified to the combined void, clay mineral fraction and cement matrix (coloured markers). Clays and silica (Opal-CT) cement are estimated to contain 60 % and 70 % intragranular porosity, respectively. XCT øt vertical error bars correspond to a combined segmentation-based error (hence the anomaly for sample St1 imaged at 5 µm) and error associated with a 10 % uncertainty in the clay and cement intragranular

porosity estimates. (b) XCT k_v data points are shown for five different image-based calculations described in Table 6: Interpolated from multiple subvolumes – blue square, numerical coarsening – blue cross, pore network modelling – red cross and upscaling using Matlab Reservoir Simulation Toolbox (MRST) – harmonic-arithmetic mean (green diamond) and harmonic mean (green triangle). XCT k_v vertical error bars correspond to the permeability values estimated and extrapolated from the lines of best fit from Figure 11, within a porosity error range of ±2 %.

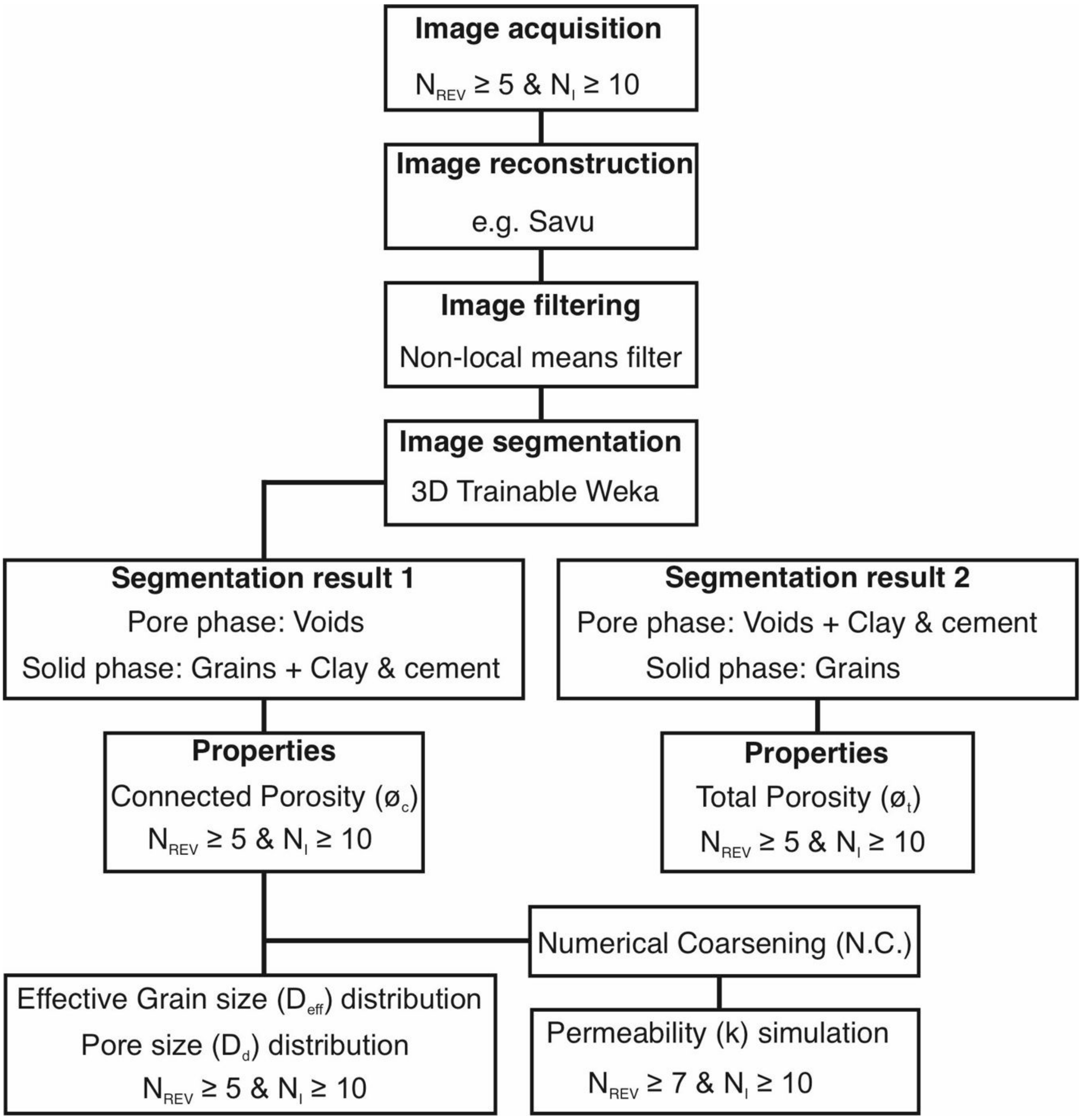

Figure 15. An optimal image processing workflow devised for porosity-permeability analysis of sandstone rock. N_{REV} is the ratio of sample length (L) to effective grain size diameter (D_{eff}), and N_I is the ratio of dominant pore throat size (D_d) to image voxel size (Δx). See Eqs (1-3) in the main text.

Appendix A. Additional Image acquisition and reconstruction information

Data was acquired using a pink beam in the energy range of 20-30 KeV. At this energy, the absorption was around 80%. Region of interest (ROI) scans were performed using a 4x optic and PCO Edge 5.5 scintillator-coupled detector in full frame mode (2560 x 2160 pixels) with a magnification of 0.032, resulting in a pixel resolution of 0.81 μm. 4000 equiangular projections were acquired through 360° with an exposure time of 0.5 s per projection. Each scan took ~ 30 minutes. In addition, flat-field and dark-field correction images were taken before and after the data acquisition.

After a dark- flat-field correction, a dezinger filter was applied with tolerance of 0.4. A paganin filter was applied (Delta/Beta = 150), which is a method of propogation-based phase retrival, to improve image contrast. No raven filter was applied, as this created ring artefacts. A lens distortion correction was also applied to the scans. In addition, padding was used in order to remove the cupping effect at the outer edge of the images introduced by ROI scanning. The reconstruction was outputted to 32-bit Tiff files, totalling 57 GB per sample.

Appendix B. Additional Flow solver information

Flow simulations were computed using a Linux-based High Performance Computing (HPC) cluster (Iridis, University of Southampton), conducted using single node, 192 GB memory systems, and one GTX1080 GPU card with 32 GB memory. The memory size constrained the maximum volume sizes possible to use for the flow simulations. The larger Comsol mesh simulations were performed on high memory nodes, which required up to 360 GB memory.

The Stokes flow equation used for the Avizo flow simulation Eq. (4) assumes laminar flow conditions (low Reynolds number), and a single-phase incompressible Newtonian fluid. For the boundary conditions of the simulation, a no-slip surface is defined between the pore-solid interface. In addition, a solid plane of one voxel width is introduced parallel to the main flow direction, to ensure that fluid is contained within a closed system. Finally, an experimental set up is added onto the faces perpendicular to the flow direction to simulate a quasi-static pressure state, and to ensure the fluid flows through the whole cross sectional input/output areas. To ensure a reliable, repeatable value of permeability, the Stokes-flow simulations should coverge using a low tolerance error. For the Avizo fluid simulation, a convergence coefficient of 10-5 was used.

Appendix C. Supplementary data

Supplementary data associated with this article can be found as additional file attachments.

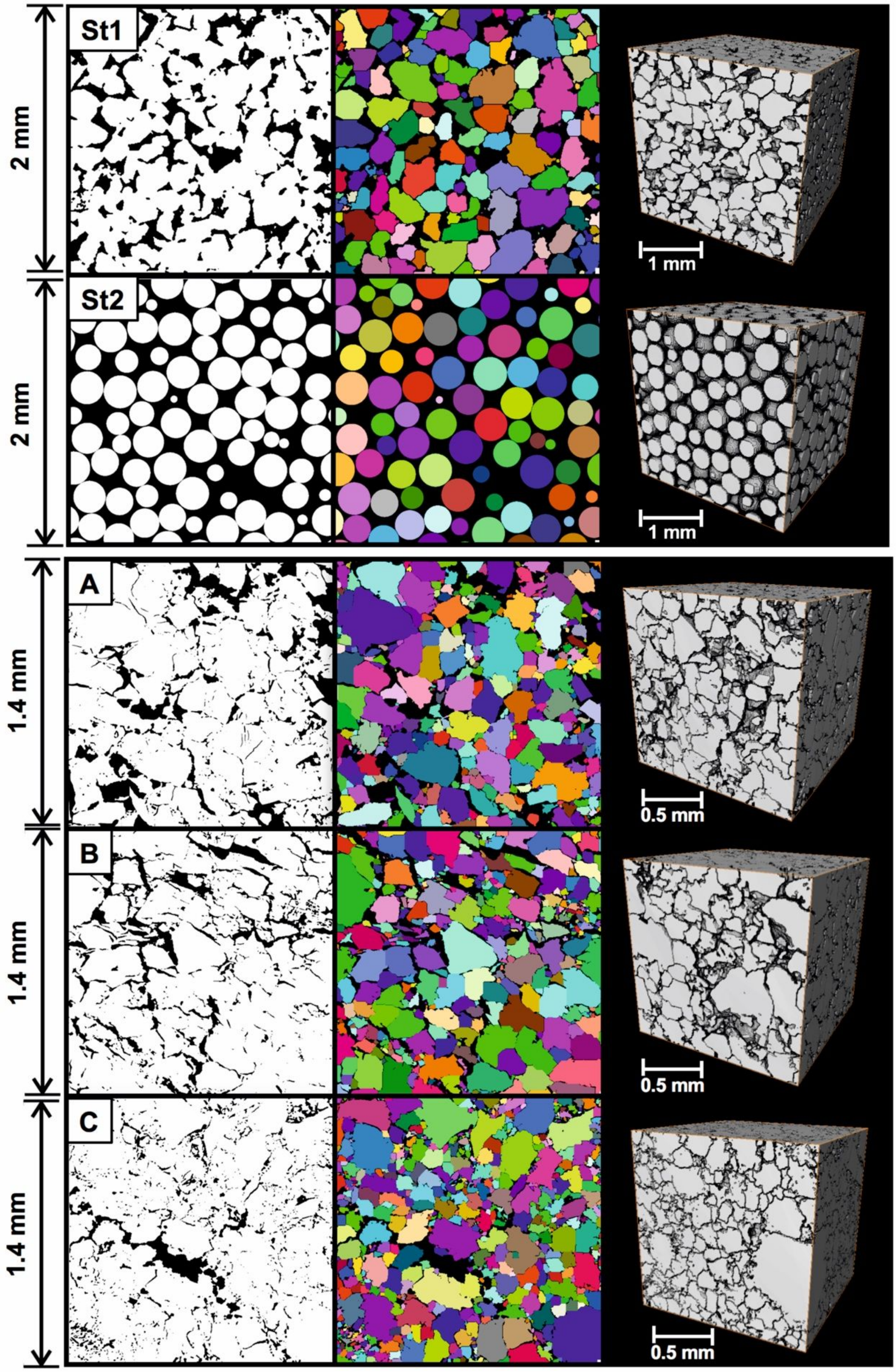

Supplementary figure: Grain Separation result for samples St1-2 and A-C. From left to right shows (1) Segmented image of pore phase (black) and solid phase (white), (2) Separated grains and 3) 3D volume of separated grains (grey).

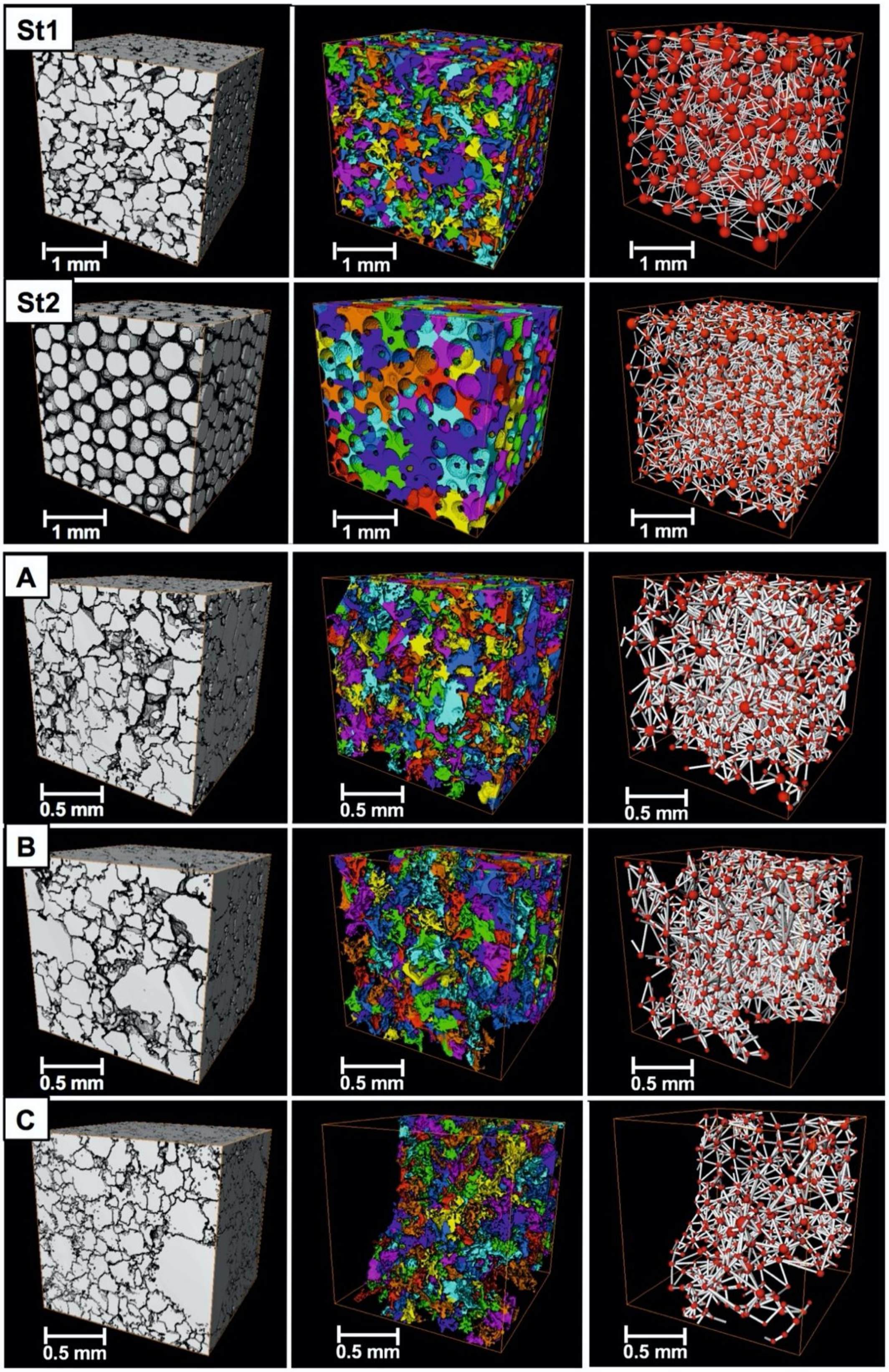

Supplementary figure: Pore separation and pore network model result for samples St1-2 and A-C. From left to right shows (1) 3D volume of separated grains (grey), (2) 3D volume of separated, connected pore phase and (3) 3D pore network model view of the connected pore phase (Pores – red; Pore throats – white).

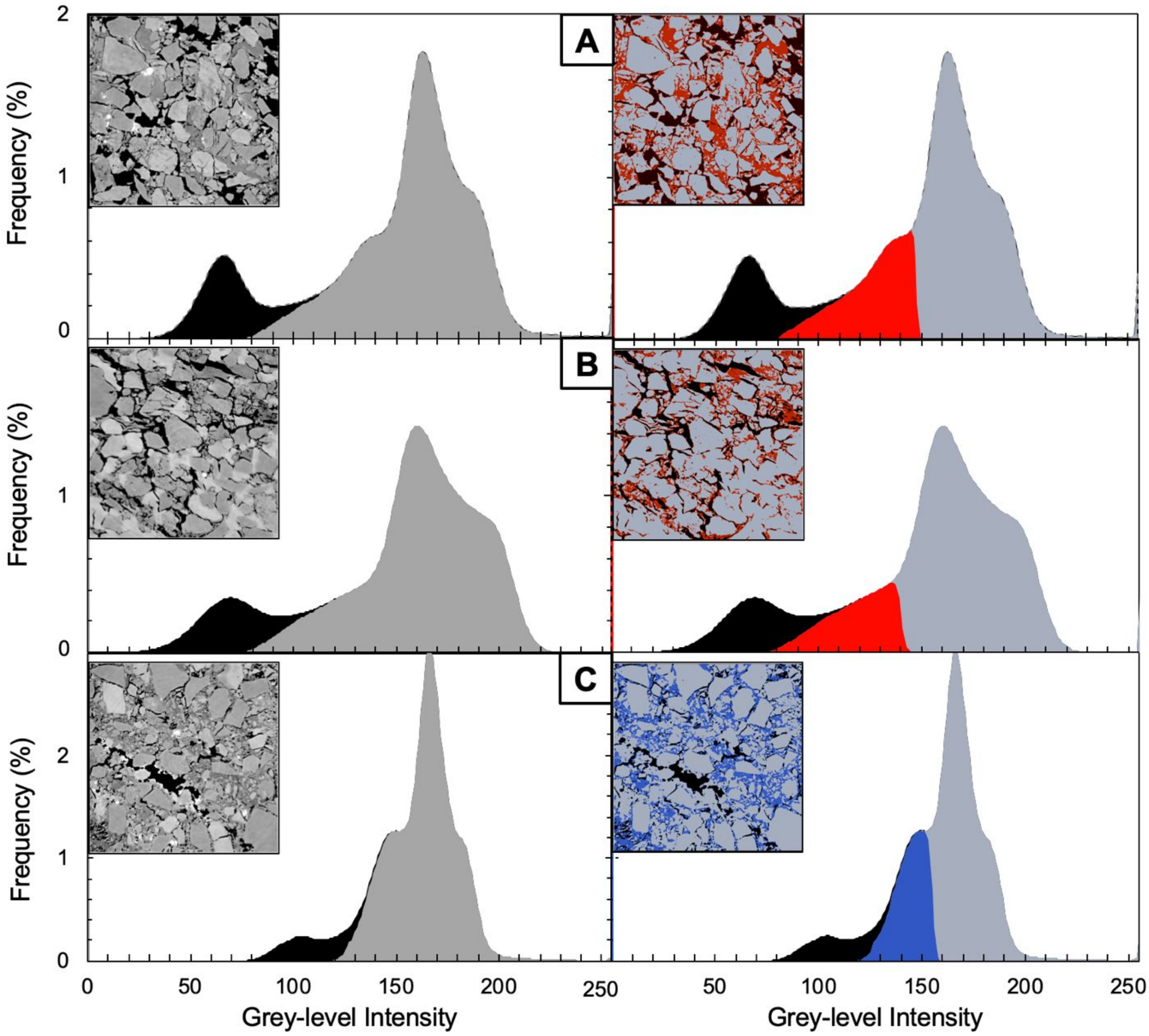

Supplementary figure: Segmentation Grey-level intensity result for samples A-C (voids – black; clay fraction – red; silica cement – blue).

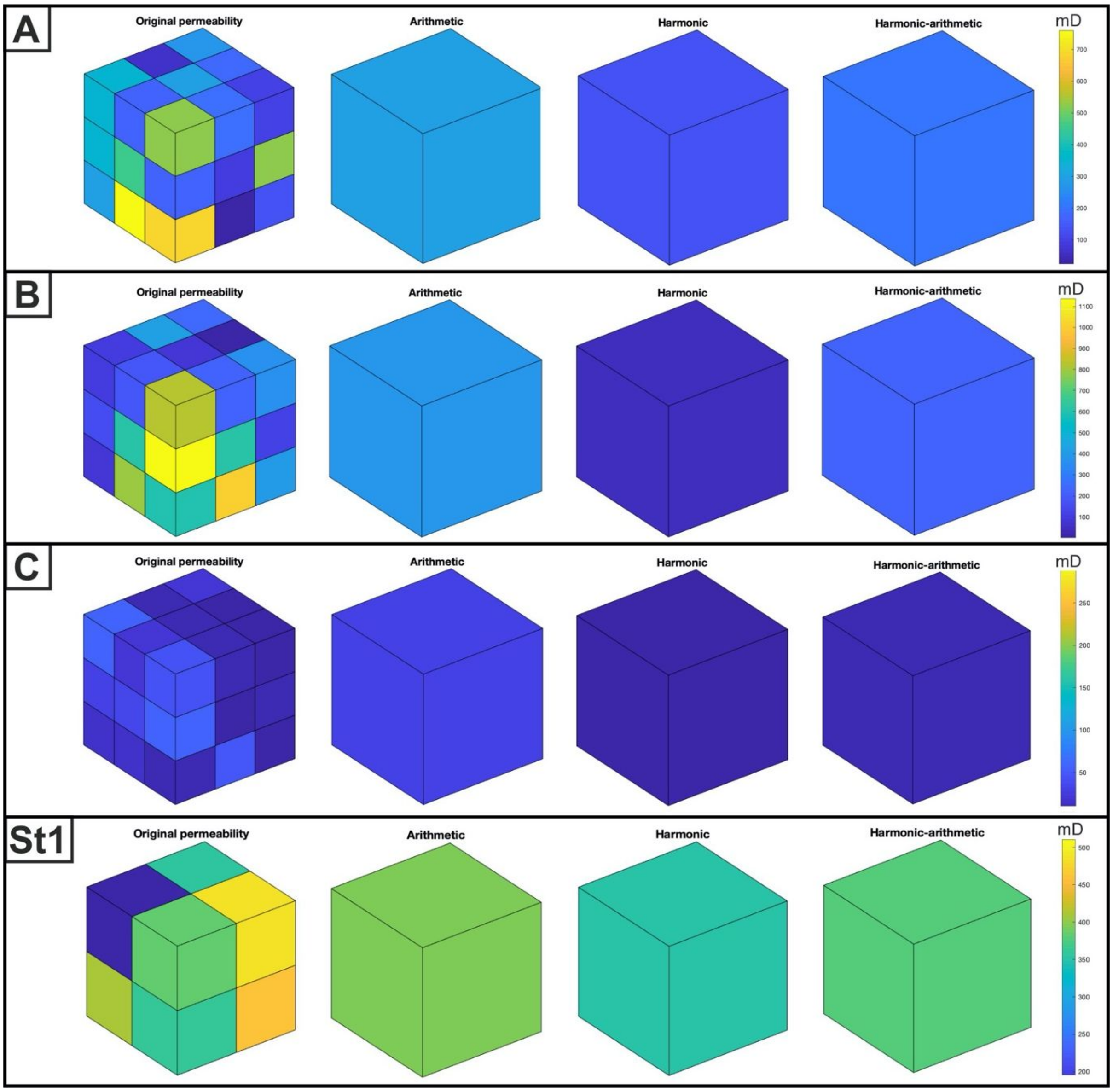

Supplementary figure: Upscaled permeability calculations of samples A, B, C and St1 using Matlab Reservoir Simulation Toolbox (MRST). Volume averaged calculations of the arithmetic, harmonic and harmonic-arithmetic means are determined.

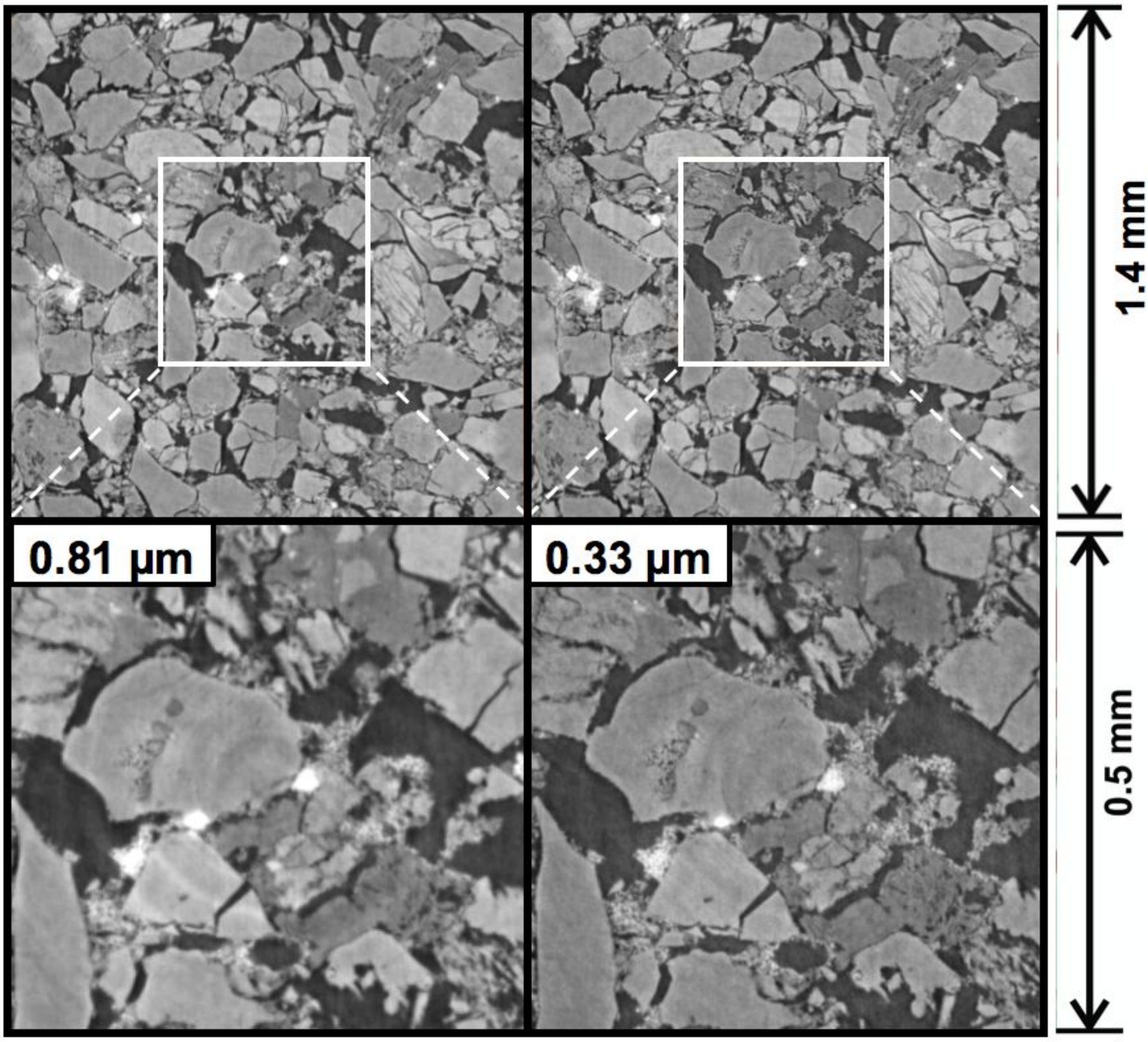

Supplementary figure: Image comparison of a 0.81 µm and 0.33 µm image spatial resolution, respectively.